PHYSICS OF PLASMAS **16**, 012101 (2009)

Antihydrogen formation from antiprotons in a pure positron plasma

Eric M. Bass and Daniel H. E. Dubin
Department of Physics, University of California, San Diego, 9500 Gilman Drive,
La Jolla, California 92093, USA

(Received 15 July 2008; accepted 10 November 2008; published online 5 January 2009)

This paper investigates the evolution in binding energy of antihydrogen atoms formed from stationary antiprotons located within a strongly magnetized positron plasma. Three-body recombination and a collisional cascade to deeper binding, limited by a kinetic bottleneck at a binding energy of $4T$, dominate the initial antihydrogen formation process. A classical Monte-Carlo simulation is used to determine the collisional transition rate between atomic binding energies, using the drift approximation for initial conditions that allow it, and full dynamics for initial conditions resulting in chaotic motion. These transition rates are employed in determining mean energy-loss rates for an ensemble of atoms, as well as in a numerical solution of the master equation to find the rate at which atoms are formed over a range of binding energies. The highly excited atoms formed by this process separate into guiding-center drift atoms and chaotic atoms. The phase-space distributions of the atoms are investigated, along with their implications for magnetic confinement and radiative energy loss. Estimates of radiative energy loss indicate that radiation is unimportant for guiding-center atoms, but increases rapidly near the chaotic regime, taking over as the dominant energy-loss process for parameters typical of recent experiments. Furthermore, the fraction of low-magnetic field seekers is considerably larger than suggested by estimates of the magnetic moment based on guiding-center dynamics, due to effects associated with chaos. © *2009 American Institute of Physics*. [DOI: 10.1063/1.3040168]

I. INTRODUCTION

Current antihydrogen formation experiments use nested Penning traps to contain a strongly magnetized, cryogenic positron plasma through which antiprotons can transit.[1,2] Bound antiproton-positron pairs formed in these traps, however, are typically far from the ground state with binding energies near the thermal level of a few Kelvin. These weakly bound atoms are characterized by slow $\mathbf{E}\times\mathbf{B}$ drift time scales, so radiation is precluded as an energy-loss mechanism until comparatively deep binding is achieved. Before this point, classical three-body collisions dominate the equilibration process. Using a Monte-Carlo simulation with classical dynamics,[4] we determine the number of bound antihydrogen atoms formed through collisions with the background positron plasma at various binding energies as a function of time. We retain finite magnetic field effects, including drift and, where relevant, cyclotron motion. The antiproton is assumed to be stationary.

After a brief review of the behavior of Rydberg atoms in strong magnetic fields, in Sec. II we consider the manner in which an ensemble of such atoms distributes itself in the available phase space, and in Sec. III discuss implications that this distribution has for magnetic confinement of the atoms. In Sec. IV we then introduce the Monte-Carlo method employed to evaluate the collisional transition rate between atomic binding energies, and in Sec. V we test the simulation using analytic theory for large impact parameter collisions. In Sec. VI we then use the results of the simulation to evaluate the mean energy-loss rate of an ensemble of atoms as a function of binding energy, and the evolution of the energy distribution of the ensemble due to collisions is considered in Sec. VII. The basic simplifying *assumption* in this analysis is that an ensemble of atomic positrons undergoing three-body recombination ergodically covers the available energy surface of bound states at any given binding energy. This allows us to follow the distribution of binding energies using a master equation with transition rates taken from the Monte-Carlo simulations. This assumption, which cannot be justified rigorously, nevertheless yields results that are in good agreement with previous work, as well as with our own simulation results. Finally, in Sec. VIII we estimate the effect that radiation has on binding energy.

When considering collisional evolution of the weakly bound atoms, the ambient positron plasma temperature T (measured in energy units) sets the energy scale. The time scale is set by the collision frequency

$$\nu = n\bar{v}b^2 = 1.3\times10^7\ \mathrm{s}^{-1}(n/10^8\ \mathrm{cm}^{-3})(T/4\ \mathrm{K})^{3/2},$$

where n is the positron plasma density, $\bar{v}=\sqrt{T/m_e}$ is the positron thermal speed, and $b=e^2/T$ is the classical distance of closest approach.

Three-body collisions continuously form bound charge pairs and re-ionize them. Previous work[3–5] indicates that such pairs are likely to remain bound only after they reach a binding energy of about $4T$, known as the kinetic bottleneck. The rate at which atoms at this energy cascade to deeper binding was found to be

$$R_3 \approx 0.07n^2\bar{v}b^5 = 7\times10^3\ \mathrm{s}^{-1}(n/10^8\ \mathrm{cm}^{-3})^2(T/4\ \mathrm{K})^{-9/2} \tag{1}$$

for the case of infinite magnetic field. The rate increases as magnetic field decreases. For zero field, the rate is about ten

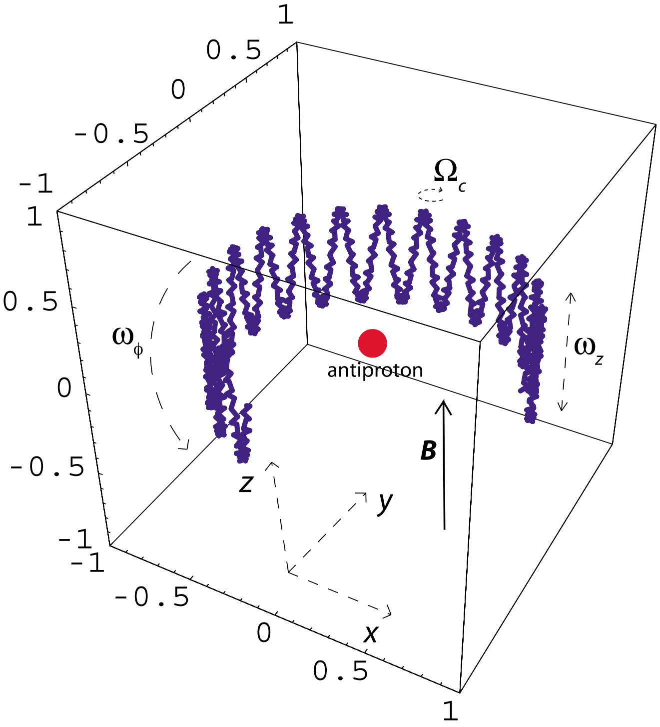

FIG. 1. (Color online) The orbital trajectory of a guiding-center atom. Here, $r_{\mathrm{cp}} < \rho < r_{\mathrm{ca}}$. The positron $\mathbf{E}\times\mathbf{B}$ drifts about the antiproton and bounces along the z-axis. The antiproton is assumed stationary for simplicity. Also, perpendicular kinetic energy is neglected ($\mathbf{E}\times\mathbf{B}$ drift approximation).

times larger than Eq. (1).[3] For a large finite field, the result is about 1.5 times larger.[5] However, the atoms formed are charge neutral and no longer confined by the Penning trap fields. Preliminary calculations suggest that almost all charge pairs exit the trap before collisional processes cause them to become deeply bound.[7] The present work finds the same result more conclusively, but also is consistent with results by Pohl *et al.*[6] showing a small fraction of atoms which do reach deep binding.

The temperature scaling of Eq. (1) motivates the use of cryogenic temperatures for recombination experiments. Low temperature and high magnetic field place such experiments in the strongly magnetized regime defined by the magnetization parameter χ, where

$$\chi \equiv \frac{\bar{v}}{b\Omega_c} = 0.0018\frac{(T/4\ \mathrm{K})^{3/2}}{(B/6\ \mathrm{T})} \ll 1, \tag{2}$$

and where $\Omega_c = eB/m_e c$ is the positron cyclotron frequency. Cross-field motion is dominated by $\mathbf{E}\times\mathbf{B}$ drift dynamics in this regime, so much of the theoretical analysis is carried out using the drift approximation.

Weakly bound atoms fall into two dynamical categories: drifting pairs (or giant dipoles) and guiding-center atoms. In the first category, transverse charge separation exceeds both the positron cyclotron radius r_{cp} and the antiproton cyclotron radius r_{ca}. The two charges drift together in the same direction, each in the electric field of the other. At slightly deeper binding, when the transverse charge separation ρ is smaller than the antiproton cyclotron radius r_{ca}, but still larger than r_{cp}, a guiding-center atom is formed (see Fig. 1). Here the positron $\mathbf{E}\times\mathbf{B}$ drifts slowly about the antiproton at frequency ω_ϕ and bounces back and forth along the magnetic field in the antiproton's electrostatic well at frequency ω_z. For small bounce motion,

$$\begin{aligned} \Omega_c &= \frac{\bar{v}}{b}\chi^{-1}, \\ \omega_z &\approx \frac{\bar{v}}{b}\epsilon^{3/2}, \\ \omega_\phi &\approx \frac{\bar{v}}{b}\chi\epsilon^{3}, \end{aligned} \tag{3}$$

where

$$\epsilon = U/T \tag{4}$$

is the binding energy U, normalized by temperature. In the limit of infinite antiproton mass, the binding energy of an atom is

$$U = \frac{e^2}{r} - \frac{1}{2}m_e(v_z^2 + v_\perp^2). \tag{5}$$

The coordinate r is the spherical radius, with the antiproton located at the origin. Note that a minus sign has been introduced so that a positive value of U indicates a bound state.

Low binding energy $[\epsilon \sim \mathcal{O}(1)]$ and large magnetic field $(\chi \ll 1)$ implies the following frequency ordering: $\Omega_c \gg \omega_z \gg \omega_\phi$. This is the regime of guiding-center drift atoms.[4] In the guiding-center drift regime, we will neglect the perpendicular velocity $\mathbf{v}_\perp$ in Eq. (5). Most perpendicular kinetic energy is bound up in the cyclotron adiabatic invariant μ_c when the atom is in the drift regime. As long as the adiabatic invariance of μ_c holds and the $\mathbf{E}\times\mathbf{B}$ drift velocity is smaller than the axial bounce velocity v_z, perpendicular kinetic energy can be ignored. The parallel action I_z is also adiabatically invariant for the frequency ordering of a guiding-center atom. There are two exact constants of the motion, which are valid in or out of the guiding-center drift approximation. They are the binding energy U and the angular momentum p_ϕ conjugate to the azimuthal coordinate,

$$p_\phi = m_e\rho^2\left(\dot{\phi} + \tfrac{1}{2}\Omega_c\right). \tag{6}$$

When normalized binding energy ϵ reaches ϵ_c, where

$$\epsilon_c = \chi^{-2/3}, \tag{7}$$

positron cyclotron motion, parallel bounce motion, and cross-field drift motion become coupled as their respective frequencies converge. This coupling marks a transition to a regime in which the atom exhibits chaotic orbits and in which electromagnetic radiation can no longer be neglected [see Fig. 2(a)]. We show, using a phase-space average of the classical Larmor power, that radiation becomes the dominant energy-loss mechanism after this transition. While the analytic theory for collisional energy loss is invalid in this regime, the simulation, which can include cyclotron motion, still applies. At still deeper binding energy, but before the atom relaxes to a low quantum n number, the magnetic field can be treated as a weak perturbation on a classical Kepler

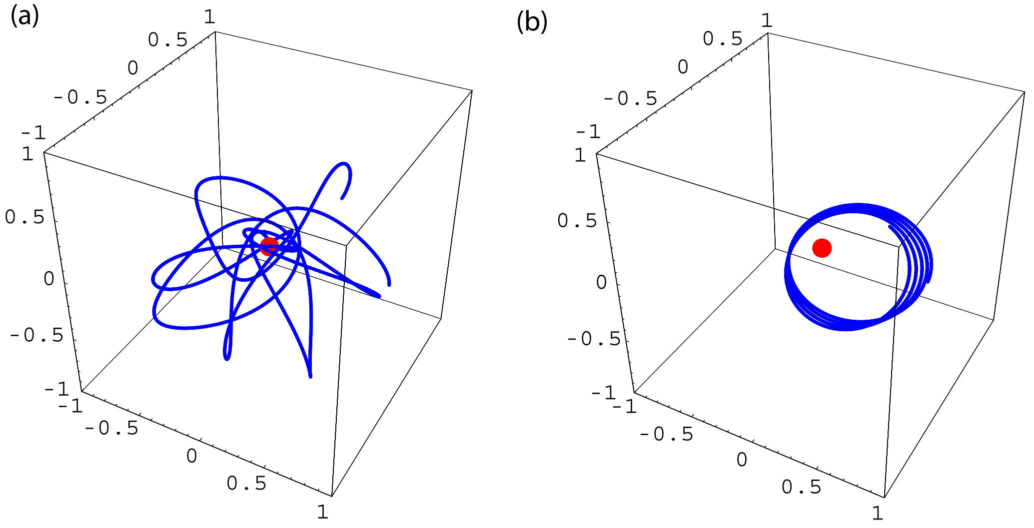

FIG. 2. (Color online) When binding energy ϵ reaches approximately $\epsilon_c = \chi^{-2/3}$, a convergence of frequencies breaks the cyclotron and bounce adiabatic invariants, leading to chaotic orbits (a). At deeper binding, the magnetic field becomes a small perturbation on a classical elliptical orbit and perturbed Kepler motion (b) results. Radiation is potentially significant in both orbital regimes.

orbit. In this regime, the plane of the elliptical orbit precesses about the magnetic field at the cyclotron frequency, as in Fig. 2(b).

II. ATOMIC DISTRIBUTIONS

In the guiding-center drift approximation, the perpendicular kinetic energy is dropped from the Hamiltonian. The normalized atomic binding energy in the guiding-center approximation then becomes

$$\epsilon_{\mathrm{GC}} = \frac{1}{\hat{r}} - \frac{1}{2}\hat{v}_z^2. \tag{8}$$

Above, and throughout the rest of the paper, a hat (^) denotes a dimensionless variable rescaled by b for length and $b/\bar{v}$ for time. For angular momentum, the dimensionless form is

$$\hat{p}_\phi = \frac{p_\phi}{m_e \bar{v} b}.$$

The adiabatically isolated perpendicular velocity is of approximately fixed magnitude and does not participate in the dynamics. Consequently, we anticipate that an ensemble of atoms at fixed energy $\epsilon_0 \ll \epsilon_c$ will be ergodically distributed over phase-space variables r and v_z, but not over the perpendicular velocity $\mathbf{v}_\perp$. This guiding-center distribution differs qualitatively from one in which all velocity variables are uniformly populated, referred to here as a three-dimensional (3D) distribution.

The guiding-center distribution P_{GC} and the three-dimensional distribution $P_{3\mathrm{D}}$ are defined as

$$P_{\mathrm{GC}}(\hat{r},\hat{v}_z) = \frac{\delta(\epsilon-\epsilon_0)\,\delta(\mathbf{v}_\perp)}{\int \delta(\epsilon-\epsilon_0)\,\delta(\mathbf{v}_\perp) 4\pi \hat{r}^2 d\hat{r}\, d^3\vec{\hat{v}}}, \tag{9}$$

$$P_{3\mathrm{D}}(\hat{r},\hat{v}) = \frac{\delta(\epsilon-\epsilon_0)}{\int \delta(\epsilon-\epsilon_0)(4\pi)^2 \hat{r}^2 \hat{v}^2 d\hat{r}\, d\hat{v}}. \tag{10}$$

In the guiding-center distribution, we have set $\mathbf{v}_\perp = 0$ for convenience. In reality the cyclotron action is expected to be fixed at the thermal level. However, perpendicular energy does not play a role in the atomic dynamics until the chaotic regime is reached, at which point the binding energy is typically much greater than T, so setting the perpendicular energy to zero rather than T does not have a significant effect on results until the chaotic regime is approached (see the discussion surrounding Fig. 6).

The distributions in the rescaled spherical radius $\hat{r}\epsilon$ illustrate the difference between guiding-center and 3D distributions:

$$P_{r\mathrm{GC}}(\hat{r}\epsilon) = \frac{1}{\epsilon}\int P_{\mathrm{GC}}(\hat{r},\hat{v}_z) 4\pi \hat{r}^2 d\hat{v}_z, \tag{11}$$

$$P_{r3\mathrm{D}}(\hat{r}\epsilon) = \frac{1}{\epsilon}\int P_{3\mathrm{D}}(\hat{r},\hat{v})(4\pi)^2 \hat{r}^2 \hat{v}^2 d\hat{v}. \tag{12}$$

The integrals in Eqs. (11) and (12) are straightforward, giving the two spherically symmetric distributions as functions of $\hat{r}\epsilon$:

$$\begin{aligned} P_{r\mathrm{GC}}(\hat{r}\epsilon) &= \frac{16}{5\pi}\frac{(\hat{r}\epsilon)^{5/2}}{\sqrt{1-\hat{r}\epsilon}}, \\ P_{r3\mathrm{D}}(\hat{r}\epsilon) &= \frac{16}{\pi}(\hat{r}\epsilon)^{3/2}\sqrt{1-\hat{r}\epsilon}. \end{aligned} \tag{13}$$

These two distributions are plotted in Fig. 3(a).

In our Monte-Carlo simulations, we sample initial conditions for the atomic positron from the guiding-center rather than the 3D distribution. At shallow binding, where guiding-center dynamics are a good approximation, this is consistent

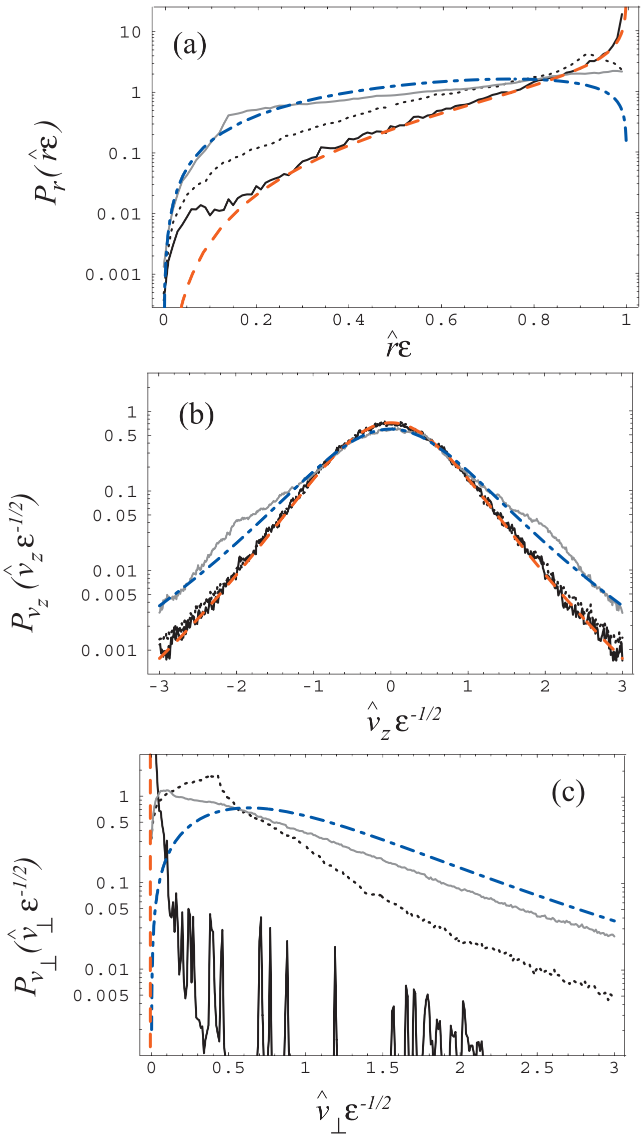

FIG. 3. (Color) The time-averaged probability density (a) P_r in the spherical radius r, (b) P_{v_z} in the velocity parallel to the magnetic field, and (c) $P_{v_\perp}$ in the magnitude of the perpendicular velocity. The plots are for $\chi=0.001$, making the chaotic cutoff $\epsilon_c=100$. The binding energies $\epsilon=4$, 35, and 100 are the solid-black, dotted-black, and solid-gray curves, respectively. The probability density is averaged over two Kepler periods and an ensemble of 500 atoms whose initial conditions are chosen from the guiding-center phase-space distribution (red, dashed curves). Full dynamics (including cyclotron motion) are used. As binding energy ϵ increases, the atom orbits naturally tend toward the fully ergodic 3D distribution (blue, dot-dashed curves).

with the basic assumption in our approach, that atomic dynamics are approximately ergodic on the energy surface. At deeper binding, this Monte-Carlo scheme still works because the chaotic nature of the atomic dynamics allows the positron orbit to sample the available energy surface so as to naturally establish a distribution qualitatively similar to the 3D distribution. This is shown in Fig. 3, which plots the distributions of an atomic ensemble in r, v_z, and $v_\perp$—each begun with the guiding-center distribution ($\mathbf{v}_\perp=0$)—averaged over time. At each binding energy, atom orbits establish a distribution that evolves from the guiding-center form to the three-dimensional form continuously as binding energy increases, to the extent allowed by conservation of p_ϕ.

Regardless of binding energy, adiabatic invariance of cyclotron action breaks if the positron orbit passes near a distance $\hat{r}_{\text{chaotic}}=1/\epsilon_c$ from the nucleus. At $\epsilon>\epsilon_c$, this condition is always met. At weaker binding, the fraction of atoms with near-nucleus orbits will also exhibit chaotic behavior, and the effect of this can be seen in Fig. 3(a) as such atoms approach the 3D distribution. Such atoms, sometimes known as helical atoms, have low angular momentum and orbits which are elongated along the magnetic field.[8]

III. MAGNETIC MOMENT

We can use ergodic distributions like the ones in Eqs. (9) and (10) to predict the average magnetic moment. Below, we determine what fraction of atoms in an ergodic ensemble would be confined by a magnetic multipole trap. When considering atomic orbits in the absence of collisions, let us adopt a second set of dimensionless units, similar to the collisional units used above but with binding energy U taking the place of T. A $(\check{\ })$ denotes units rescaled by

(e^2/U) for length,

$(e^2/U)\sqrt{m_e/U}$ for time, and

$m_e\sqrt{U/m_e}$ for momentum.

Note that $\check{\Omega}_c$ in these units is related to χ and ϵ by

$$\check{\Omega}_c=(\chi\epsilon^{3/2})^{-1}.$$

The chaotic orbit condition of Eq. (7) becomes $\check{\Omega}_c=1$. When $\check{\Omega}_c\gg 1$, the atom is in the guiding-center drift orbit regime. When $\check{\Omega}_c\ll 1$, the orbit is nearly Keplerian.

The atom will be confined within a magnetic mirror trap if the time-averaged magnetic moment μ_z is negative. The instantaneous magnetic moment is proportional to the kinematic angular momentum,[9] so the time-averaged kinematic angular momentum must also be negative:

$$\frac{2\sqrt{Um_e}}{e^3}\langle\mu_z\rangle=\langle\check{L}_z\rangle=\left\langle\check{p}_\phi-\frac{1}{2}\check{\rho}^2\check{\Omega}_c\right\rangle<0.$$

The angular momentum $\check{p}_\phi$ is conserved and can be removed from the average. The confinement condition then becomes

$$\check{p}_\phi-\tfrac{1}{2}\check{\Omega}_c\langle\check{\rho}^2\rangle<0. \tag{14}$$

The average in Eq. (14) is over time for a single positron trajectory. We can replace this time average with a phase-space average over the surface traced out by the orbit. For a single trajectory, both energy U and angular momentum p_ϕ are conserved. In the guiding-center orbit regime, the cyclotron magnetic moment μ_c is also conserved. Let us assume that the positron ergodically covers the surface defined by fixing the appropriate parameters: p_ϕ, U, and μ_c in the case of guiding-center atoms; p_ϕ and U in chaotic atoms. We will address each case separately, beginning with guiding-center atoms.

The fixed cyclotron action μ_c expressed in orbital $(\check{\ })$ units is

$$\check{\mu}_c = \frac{(\check{\mathbf{v}}_\perp - \check{\mathbf{v}}_{\mathbf{E}\times\mathbf{B}})^2}{\check{\Omega}_c}.$$

The perpendicular velocity $\check{\mathbf{v}}_\perp$ and the instantaneous drift velocity $\check{\mathbf{v}}_{\mathbf{E}\times\mathbf{B}}$ are given in cylindrical coordinates by

$$\check{\mathbf{v}}_\perp = \check{p}_\rho \vec{a}_\rho + \left(\frac{\check{p}_\phi}{\check{\rho}} - \frac{1}{2}\check{\rho}\check{\Omega}_c\right)\vec{a}_\phi,$$

$$\check{\mathbf{v}}_{\mathbf{E}\times\mathbf{B}} = \check{\rho}\check{\varpi}_\phi \vec{a}_\phi.$$

Above, $\check{p}_\alpha$ is the canonical momentum associated with coordinate α and $\vec{a}_\alpha$ is the unit vector along α. The instantaneous drift frequency

$$\check{\varpi}_\phi = \frac{1}{\check{\Omega}_c(\check{\rho}^2 + \check{z}^2)^{3/2}}.$$

The quantities above order as follows with respect to the large parameter $\check{\Omega}_c$:

$$\check{p}_\phi \quad : \quad \mathcal{O}(\check{\Omega}_c),$$

$$\check{\rho}, \check{z}, \left(\frac{\check{p}_\phi}{\check{\rho}} - \frac{1}{2}\check{\rho}\check{\Omega}_c\right) \quad : \quad \mathcal{O}(1),$$

$$\check{\mu}_c, \check{\varpi}_\phi \quad : \quad \mathcal{O}(1/\check{\Omega}_c).$$

Fixing the guiding-center binding energy, given by

$$\check{U}_{\mathrm{GC}} = \frac{1}{(\check{\rho}_0^2 + \check{z}^2)^{1/2}} - \frac{1}{2}\check{p}_z^2 = 1,$$

as well as angular momentum $\check{p}_\phi$ and cyclotron action $\check{\mu}_c$ defines the phase-space surface over which the average in Eq. (14) is taken. Above, $\check{\rho}_0 = \sqrt{2\check{p}_\phi/\check{\Omega}_c}$ is the fixed guiding-center radius from the large Ω_c limit of Eq. (6). The phase-space average is expressed as

$$\langle \check{\rho}^2 \rangle = \frac{\displaystyle\int \check{\rho}^2 \delta(\check{U}_{\mathrm{GC}} - 1)\,\delta\left[\check{\Omega}_c\check{\mu}_c - \check{p}_\rho^2 - \left(\frac{\check{p}_\phi}{\check{\rho}} - \frac{1}{2}\check{\rho}\check{\Omega}_c - \check{\rho}\check{\varpi}_\phi\right)^2\right] d\check{p}_\rho d\check{p}_z d\check{z} d\check{\rho}}{\displaystyle\int \delta(\check{U}_{\mathrm{GC}} - 1)\,\delta\left[\check{\Omega}_c\check{\mu}_c - \check{p}_\rho^2 - \left(\frac{\check{p}_\phi}{\check{\rho}} - \frac{1}{2}\check{\rho}\check{\Omega}_c - \check{\rho}\check{\varpi}_\phi\right)^2\right] d\check{p}_\rho d\check{p}_z d\check{z} d\check{\rho}}.$$

Upon performing integrals over $\check{p}_\rho$ and $\check{p}_z$, we obtain the following expression:

$$\langle \check{\rho}^2 \rangle = \frac{\displaystyle\int \frac{\check{\rho}^2}{\sqrt{\check{\Omega}_c\check{\mu}_c - \left[\dfrac{\check{p}_\phi}{\check{\rho}} - \dfrac{1}{2}\check{\rho}(\check{\Omega}_c + 2\check{\varpi}_\phi)\right]^2}} \frac{(\check{\rho}_0^2 + \check{z}^2)^{1/4}}{\sqrt{1 - (\check{\rho}_0^2 + \check{z}^2)^{1/2}}} d\check{\rho} dz}{\displaystyle\int \frac{1}{\sqrt{\check{\Omega}_c\check{\mu}_c - \left[\dfrac{\check{p}_\phi}{\check{\rho}} - \dfrac{1}{2}\check{\rho}(\check{\Omega}_c + 2\check{\varpi}_\phi)\right]^2}} \frac{(\check{\rho}_0^2 + \check{z}^2)^{1/4}}{\sqrt{1 - (\check{\rho}_0^2 + \check{z}^2)^{1/2}}} d\check{\rho} dz}. \tag{15}$$

Cyclotron oscillations in the cylindrical radius $\check{\rho}$ about the guiding-center value $\check{\rho}_0 = \sqrt{2\check{p}_\phi/\check{\Omega}_c}$ are of order $(1/\check{\Omega}_c)$. Let us neglect the effect these small oscillations have on the already small $[\mathcal{O}(1/\check{\Omega}_c)]$ instantaneous drift frequency and approximate

$$\check{\varpi}_\phi \simeq \frac{1}{\check{\Omega}_c(\check{\rho}_0^2 + \check{z}^2)^{3/2}}.$$

The integral over $\check{\rho}$ in Eq. (15) can then be performed analytically. The integration domain is

$$\check{\rho}_1 - \frac{(\check{\Omega}_c\check{\mu}_c)^{1/2}}{\check{\Omega}_c + 2\check{\varpi}_\phi} \leqslant \check{\rho} \leqslant \check{\rho}_1 + \frac{(\check{\Omega}_c\check{\mu}_c)^{1/2}}{\check{\Omega}_c + 2\check{\varpi}_\phi},$$

with

$$\check{\rho}_1 = \frac{\sqrt{2\check{p}_\phi(\check{\Omega}_c + 2\check{\varpi}_\phi) + \check{\Omega}_c\check{\mu}_c}}{\check{\Omega}_c + 2\check{\varpi}_\phi}.$$

As $\check{\Omega}_c \to \infty$, the left and right limits converge on the guiding-center radius $\check{\rho}_0$. After performing the integration along $\check{\rho}$, we obtain

$$\langle \check{\rho}^2 \rangle = \frac{\displaystyle 2\int \frac{\check{\mu}_c + \check{p}_\phi}{\check{\Omega}_c + 2\check{\varpi}_\phi} \frac{(\check{\rho}_0^2 + \check{z}^2)^{1/4}}{\sqrt{1 - (\check{\rho}_0^2 + \check{z}^2)^{1/2}}} d\check{z}}{\displaystyle\int \frac{(\check{\rho}_0^2 + \check{z}^2)^{1/4}}{\sqrt{1 - (\check{\rho}_0^2 + \check{z}^2)^{1/2}}} d\check{z}}.$$

Expanding the integrand above and keeping terms up to $\mathcal{O}(1/\check{\Omega}_c^2)$ gives

$$\langle\check{\rho}^2\rangle \simeq \frac{2}{\check{\Omega}_c}\left(\check{p}_\phi + \check{\mu}_c - \rho_0^2\frac{\int \check{\varpi}_\phi \frac{(\check{\rho}_0^2+\check{z}^2)^{1/4}}{\sqrt{1-(\check{\rho}_0^2+\check{z}^2)^{1/2}}}d\check{z}}{\int \frac{(\check{\rho}_0^2+\check{z}^2)^{1/4}}{\sqrt{1-(\check{\rho}_0^2+\check{z}^2)^{1/2}}}d\check{z}}\right).$$

Finally, we note that the integrand in the denominator of the third term is proportional to the integral of the original phase-space distribution over all variables but $\check{z}$. This factor is therefore the appropriate weighting factor in taking an average over $\check{z}$. Returning to Eq. (14), we obtain the confinement condition in the guiding-center drift regime:[10]

$$\check{p}_\phi - \tfrac{1}{2}\check{\Omega}_c\langle\check{\rho}^2\rangle = \check{\rho}_0^2\check{\omega}_\phi - \check{\mu}_c \leqslant 0,$$

which implies that

$$\check{\mu}_c \geqslant \check{\rho}_0^2\check{\omega}_\phi \tag{16}$$

is required for confinement. Above, the bounce-average drift frequency $\check{\omega}_\phi$ is given by

$$\check{\omega}_\phi = \frac{\int \frac{1}{(\check{\rho}_0^2+\check{z}^2)^{3/2}}\frac{(\check{\rho}_0^2+\check{z}^2)^{1/4}}{\sqrt{1-(\check{\rho}_0^2+\check{z}^2)^{1/2}}}d\check{z}}{\check{\Omega}_c\int \frac{(\check{\rho}_0^2+\check{z}^2)^{1/4}}{\sqrt{1-(\check{\rho}_0^2+\check{z}^2)^{1/2}}}d\check{z}}.$$

The left side of Eq. (16) is the magnetic moment due to cyclotron motion, which favors confinement. The right side is the magnetic moment due to the **E**×**B** drift orbit, which opposes confinement.

The fraction N_{trapGC} of such confined atoms is given by an integral of the atomic distribution over the μ_c and p_ϕ parameters that give confinement. The magnetic moments $\check{\mu}_c$ are distributed according to the thermal distribution

$$P_\mu(\check{\mu}_c) = \frac{\check{\Omega}_c U}{2T}e^{-\check{\Omega}_c\check{\mu}_c U/2T} = \frac{\check{\Omega}_c\epsilon}{2}e^{-\check{\Omega}_c\epsilon\check{\mu}_c/2}.$$

Let us assume that the angular momenta are distributed ergodically on the guiding-center energy surface:

$$\begin{aligned}P_{p_\phi\text{GC}}(\check{p}_\phi) &= \frac{\int\delta(\check{U}_{\text{GC}}-1)d\check{\rho}d\check{z}d\check{p}_\rho d\check{p}_z}{\int\delta(\check{U}_{\text{GC}}-1)d\check{\rho}d\check{z}d\check{p}_\rho d\check{p}_z d\check{p}_\phi}\\ &= \frac{16}{5\pi\check{\Omega}_c}\int_0^{\sqrt{1-2\check{p}_\phi/\check{\Omega}_c}}\frac{\left(\frac{2\check{p}_\phi}{\check{\Omega}_c}+\check{z}^2\right)^{1/4}}{\sqrt{1-\left(\frac{2\check{p}_\phi}{\check{\Omega}_c}+\check{z}^2\right)^{1/2}}}d\check{z}.\end{aligned} \tag{17}$$

Above we made the substitution $\check{\rho}_0^2=2\check{p}_\phi/\check{\Omega}_c$. According to Eq. (16), the fraction of atoms that are magnetically confined is

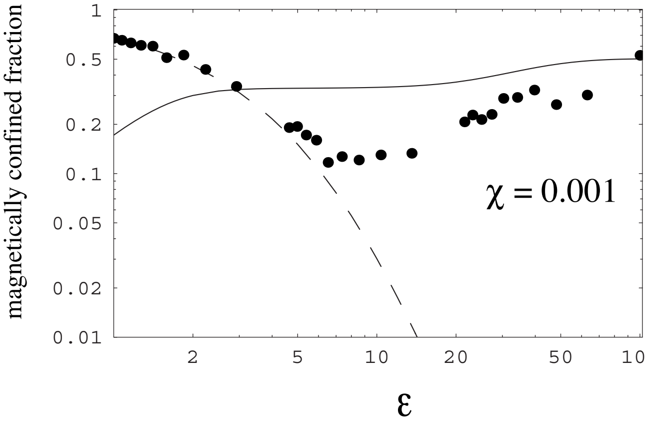

FIG. 4. The predicted fraction of atoms with a magnetic moment favoring confinement by a magnetic trap ($\mu_z<0$) as a function of ϵ (on a log-log scale) for $\chi=0.001$. The dashed and solid curves represent predictions in the guiding-center and chaotic atom regimes, respectively. The dots show the confined fraction of 1000 simulated atoms distributed ergodically in guiding-center phase space with cyclotron action distributed thermally. As binding energy increases, atoms switch to the chaotic distribution and confinement improves.

$$\begin{aligned}N_{\text{trapGC}} &= \frac{\check{\Omega}_c\epsilon}{2}\int_0^{\check{\Omega}_c/2}d\check{p}_\phi\int_{2\check{p}_\phi/\bar{\Omega}_c\check{\omega}_\phi}^{\infty}d\check{\mu}_c e^{-\check{\Omega}_c\epsilon\check{\mu}_c/2}P_{p_\phi\text{GC}}(\check{p}_\phi)\\ &= \int_0^{\check{\Omega}_c/2}e^{-\epsilon\check{p}_\phi\check{\omega}_\phi}P_{p_\phi\text{GC}}(\check{p}_\phi)d\check{p}_\phi.\end{aligned} \tag{18}$$

This fraction is shown at $\chi=0.001$ as a function of ϵ in Fig. 4 (dashed curve). As guiding-center atoms become more deeply bound relative to the thermal energy, the confined fraction decreases drastically, because the magnetic moment associated with **E**×**B** drift motion increases. We see next that this condition improves once atoms pass into the regime of chaotic orbits and the cyclotron action μ_c is no longer at the thermal level, as perpendicular energy is shared with the other degrees of freedom.

In the chaotic regime, the cyclotron adiabatic invariant is broken. In this case, the average in Eq. (14) should be taken over the phase-space surface defined by fixing energy and p_ϕ only. The three-dimensional energy $\check{U}_{3\text{D}}$ is now used:

$$\check{U}_{3\text{D}} = \frac{1}{(\check{\rho}^2+\check{z}^2)^{1/2}} - \frac{1}{2}\left[\check{p}_z^2+\check{p}_\rho^2+\left(\frac{\check{p}_\phi}{\check{\rho}}-\frac{1}{2}\check{\rho}\check{\Omega}_c\right)^2\right] = 1.$$

The average $\langle\check{\rho}^2\rangle$ at fixed energy and angular momentum $\check{p}_\phi$ is given by

$$\langle\check{\rho}^2\rangle = \frac{\int\check{\rho}^2\delta(\check{U}_{3\text{D}}-1)d\check{\rho}d\check{z}d\check{p}_\rho d\check{p}_z}{\int\delta(\check{U}_{3\text{D}}-1)d\check{\rho}d\check{z}d\check{p}_\rho d\check{p}_z}.$$

In both the numerator and denominator, all but one of the integrals can be done analytically and the expression reduces to

$$\langle \check{\rho}^2 \rangle = \frac{\displaystyle\int_{\check{\rho}_{\min}}^{\check{\rho}_{\max}} \check{\rho}^2 \sqrt{4\left[2+\left(\frac{\check{p}_\phi}{\check{\rho}}-\frac{1}{2}\check{\rho}\check{\Omega}_c\right)^2\right]^{-2}-\check{\rho}^2}\,d\check{\rho}}{\displaystyle\int_{\check{\rho}_{\min}}^{\check{\rho}_{\max}} \sqrt{4\left[2+\left(\frac{\check{p}_\phi}{\check{\rho}}-\frac{1}{2}\check{\rho}\check{\Omega}_c\right)^2\right]^{-2}-\check{\rho}^2}\,d\check{\rho}}. \tag{19}$$

Above, the limits $\check{\rho}_{\min}$ and $\check{\rho}_{\max}$ are determined by the positive, real roots of

$$4\left[2+\left(\frac{\check{p}_\phi}{\check{\rho}}-\frac{1}{2}\check{\rho}\check{\Omega}_c\right)^2\right]^{-2}-\check{\rho}^2=0.$$

The confinement condition of Eq. (14), combined with Eq. (19), defines the values of $\check{p}_\phi$ for which chaotic atoms are confined for a given value of $\check{\Omega}_c$. This includes all available values of $\check{p}_\phi$ below some $\check{p}_{\phi\text{con}}$. The magnetically confined fraction N_{trap3D} of chaotic atoms is the integral of $P_{p_\phi 3\text{D}}(\check{p}_\phi)$ over the confined domain:

$$N_{\text{trap3D}} = \int_{\check{p}_{\phi\min}}^{\check{p}_{\phi\text{con}}} P_{p_\phi 3\text{D}}(\check{p}_\phi)\,d\bar{p}_\phi. \tag{20}$$

The ergodic distribution of angular momenta in the chaotic regime is given by

$$\begin{aligned} P_{p_\phi 3\text{D}}(\check{p}_\phi) &= \frac{\int \delta(\check{U}_{3\text{D}}-1)\,d\check{\rho}\,d\check{z}\,d\check{p}_\rho\,d\check{p}_z}{\int \delta(\check{U}_{3\text{D}}-1)\,d\check{\rho}\,d\check{z}\,d\check{p}_\rho\,d\check{p}_z\,d\check{p}_\phi} \\ &= \frac{4\sqrt{2}}{\pi}\int_{\check{\rho}_{\max}}^{\check{\rho}_{\min}} \sqrt{4\left[2+\left(\frac{\check{p}_\phi}{\check{\rho}}-\frac{1}{2}\check{\rho}\check{\Omega}_c\right)^2\right]^{-2}-\check{\rho}^2}\,d\check{\rho}. \end{aligned} \tag{21}$$

The solid curve in Fig. 4 shows the predicted fraction of confined atoms for $\chi=0.001$ as a function of ϵ in the chaotic regime. The dots in the figure show the fraction of 1000 simulated atoms with an average kinematic angular momentum $\langle L_z \rangle$ indicating confinement. The atom initial conditions are populated as is appropriate for the guiding-center regime, but full three-dimensional dynamics are followed. At low energies, the confined fraction matches the guiding-center prediction. At deeper binding, the cyclotron adiabatic invariant breaks and the confined fraction converges on the chaotic prediction. At deep binding, both the simulated atoms and the chaotic prediction converge on a confined fraction of 0.5. In this range atoms are effectively unmagnetized and are equally likely to be in a confined or unconfined state.

IV. SIMULATION PROCEDURE

As discussed in Sec. I, we investigate three-body recombination using a numerical simulation based on classical dynamics. The simulation follows the dynamics of a bound positron with a given initial binding energy as it collides with an unbound positron, chosen randomly from a positron plasma at temperature T.

The simulation consists of many independent, single-collision events whose initial conditions are taken from the same distribution. Each collision's initial and final conditions are saved for analysis. Initial conditions in each collision are always randomly regenerated, not saved from event to event. Around 20 000–100 000 collisions are performed for each initial atomic binding energy chosen.

Each independent shot in the simulation begins using the guiding-center equations of motion, but will switch to three-dimensional (i.e., cyclotron inclusive) dynamics if the distance between any two of the three charges (bound positron, free positron, and antiproton nucleus) becomes less than $2\hat{r}_{\text{chaotic}}=2\chi^{2/3}$. When charges are separated by the chaotic cutoff radius r_{chaotic}, the instantaneous $\mathbf{E}\times\mathbf{B}$ drift orbit frequency is equal to the cyclotron frequency Ω_c and cyclotron action is no longer a good adiabatic invariant. If activated, full dynamics remain on for the duration of the simulated collision. This approach is required to conserve energy.

Initial conditions for the bound positron are chosen from the guiding-center ergodic distribution of Eq. (9) at each fixed binding energy. As discussed above, the distribution evolves toward the form appropriate for the atomic binding energy before the collision occurs.

For the free positron, the initial parallel velocity in every shot is chosen from a weighted Maxwellian distribution at temperature T given by

$$f(v_z) \propto |v_z| e^{-v_z^2/2\bar{v}^2}.$$

If the simulation switches over to full dynamics, the perpendicular velocities of both the free and bound positrons begin at zero, conserving total energy and canonical angular momentum p_ϕ. Setting the free particle's initial perpendicular kinetic energy to zero is equivalent to setting the positron plasma perpendicular temperature to zero. The effect of this choice is a slight enhancement of the cascade to deep binding, as discussed in relation to Fig. 6. However, in some high-B and low temperature trap configurations, a two-temperature distribution $(T_\perp \ll T_\parallel)$ may be physical, since cyclotron cooling affects only the perpendicular temperature while heating due to field errors acts mainly on the parallel temperature. Furthermore, perpendicular to parallel temperature equilibration is exponentially suppressed in the strongly magnetized regime $\chi \ll 1$.[11]

The free positron's initial position relative to the guiding-center atom orbit is chosen with equal probability for equal area, with radius restricted to $0<\hat{r}_p<10/\epsilon_0$, where ϵ_0 is the initial binding energy.

We must initially place the impacting positron far enough away in z to approximate a collision from infinity. The distance is largest for large impact parameter collisions. As the free positron approaches the atom, the bound positron's drift orbit becomes distorted, resulting in fluctuations in the orbit's cylindrical radius ρ with period ω_ϕ (the drift frequency) and magnitude of order

$$\delta\hat{\rho} = \frac{\hat{\rho}^3\hat{\rho}_p}{\hat{z}_p^3},$$

where $\hat{\rho}_p$ and $\hat{z}_p$ are the cylindrical radius and axial position, respectively, of the free positron. The predicted step in cylindrical radius $\Delta\hat{\rho}$ for a large impact parameter collision comes from an integral over unperturbed orbits [Eq. (43) below]. For appropriate accuracy, we require that

$\Delta\hat\rho \gg \delta\hat\rho_{\min}$, where $\delta\hat\rho_{\min}$ occurs at $\hat z_{\text{limit}}$. Choosing $\sin(\phi) = -1/2$ for simplicity, we obtain

$$\hat z_{\text{limit}}^2 \gg \frac{\hat\rho_p \hat\rho^6 \hat v_z^2}{\chi^2 K_1\left(\left|\dfrac{\hat\omega_\phi \hat\rho_p}{\hat v_z}\right|\right)}. \tag{22}$$

The free positron is initially placed at least ten times the $\hat z$ separation dictated by Eq. (22) and the run is ended when either positron reaches the same $\hat z$-separation again.

V. COLLISIONAL TRANSITION PROBABILITY RATE DENSITY

The previously described simulation has been used to numerically evaluate $w(\epsilon,\epsilon')$, the collisional transition rate of an atom from energy ϵ to energy ϵ' averaged over all other variables. Since atom orbits appear to fill phase space in a qualitatively ergodic manner (Fig. 3), we consider only the evolution of the distribution $f(\epsilon)$ in this variable, with the assumption that all other variables are populated ergodically. In Sec. VII we will use $w(\epsilon,\epsilon')$ to determine the collisional evolution of a distribution of weakly bound atoms to deeper binding. In Sec. VIII, we consider atomic evolution due to radiation.

In order to connect the simulation results to $\omega(\epsilon,\epsilon')$, consider the master equation for the collisional time evolution of $f(\epsilon)$:

$$\frac{\partial f}{\partial t} = \int [f(\epsilon')w(\epsilon',\epsilon) - f(\epsilon)w(\epsilon,\epsilon')]d\epsilon'. \tag{23}$$

For any transition probability rate density $w(\epsilon,\epsilon')$,

$$\int w(\epsilon,\epsilon')d\epsilon' \equiv \nu_{\text{eff}} = \frac{\text{total number of events}}{\text{time}}.$$

The rate extracted from the simulation includes collisions within a disk of radius

$$\hat\rho_{\max} = \frac{10}{\epsilon},$$

or ten times the atom radius, for each initial binding energy considered. The effective collision frequency ν_{eff} is then

$$\nu_{\text{eff}} = n\bar v b^2 \pi \hat\rho_{\max}^2 \frac{\int_{-\infty}^{\infty} |\hat v_z| e^{-\hat v_z^2/2} d\hat v_z}{\int_{-\infty}^{\infty} e^{-\hat v_z^2/2} d\hat v_z} = n\bar v b^2 \sqrt{2\pi}\frac{100}{\epsilon^2}. \tag{24}$$

To extract $w(\epsilon,\epsilon')$, consider the evolution of a delta function $f(\epsilon)|_{t=0} = \delta(\epsilon-\epsilon_0)$ (our initial condition in the simulations) after a short time Δt:

$$f(\epsilon)|_{t=\Delta t} = \delta(\epsilon-\epsilon_0) + \left.\frac{\partial f}{\partial t}\right|_{t=0} \Delta t.$$

Substituting Eq. (23) into this expression gives

$$f(\epsilon)|_{t=\Delta t} = \delta(\epsilon-\epsilon_0) + \Delta t w(\epsilon_0,\epsilon) - \nu_{\text{eff}}\Delta t \delta(\epsilon-\epsilon_0). \tag{25}$$

Recall that ν_{eff} [Eq. (24)] is the effective collision frequency for all considered collisions. In time Δt, the probability P_n of an atom undergoing n collisions is given by a Poisson distribution,

$$P_n = \frac{(\nu_{\text{eff}}\Delta t)^n}{n!} e^{-\nu_{\text{eff}}\Delta t}.$$

For very short times Δt,

$$P_0 = 1 - \nu_{\text{eff}}\Delta t,$$

$$P_1 = \nu_{\text{eff}}\Delta t,$$

$$P_n = O(\Delta t^n), \quad n > 1,$$

and the distribution is given to first order in Δt by

$$f(\epsilon)|_{t=\Delta t} = P_0 f_0 + P_1 f_1,$$

where f_0 is the original distribution and f_1 is the normalized distribution of atoms that have undergone one collision. For the simulation, $f_0 = \delta(\epsilon-\epsilon_0)$ and f_1 is the final distribution in binding energy. This gives

$$f(\epsilon)|_{t=\Delta t} = (1 - \nu_{\text{eff}}\Delta t)\delta(\epsilon-\epsilon') + \nu_{\text{eff}}\Delta t f_1. \tag{26}$$

Comparing Eqs. (25) and (26) readily yields

$$w(\epsilon_0,\epsilon) = \nu_{\text{eff}} f_1. \tag{27}$$

Thus, the distribution of final states from our Monte-Carlo simulation is proportional to the transition probability rate density. Equations (25) and (26) are exact as Δt approaches zero, so Eq. (27) is exact as well.

Figure 5 shows $w(\epsilon,\epsilon')$ for $\epsilon=4$ and $\epsilon=20$. It shows that replacement collisions, where the free positron replaces the bound one, usually at deeper binding, constitute a larger fraction of collisions with large energy steps. Only a small fraction of collisions resulting in small energy steps were of this variety.

We have chosen a fit $w(\epsilon,\epsilon')$ to a function of the form

$$w(\epsilon,\epsilon') = n\bar v b^2 \times \begin{cases} [A_L(\epsilon-\epsilon')^{\alpha_L} + B_L(\epsilon-\epsilon')^{\beta_L}]^{-1} & \text{for } \epsilon' < \epsilon \\ [A_R(\epsilon'-\epsilon)^{\alpha_R} + B_R(\epsilon'-\epsilon)^{\beta_R}]^{-1} & \text{for } \epsilon' > \epsilon \end{cases} \tag{28}$$

over most of the domain. At low values of ϵ, a fit ensuring detailed balance is used (see below). The fit parameters A, B, α, and β vary for different values of ϵ. The best fit values to the simulation data are supplied in Tables I–III. To generate a smooth transition rate for all values of ϵ and ϵ' on the simulation grid used in Sec. VII, we first calculated $w(\epsilon,\epsilon')$ on every grid point (excluding the singularity at $\epsilon=\epsilon'$) using linear interpolation between the discrete ϵ fits in Tables I–III.

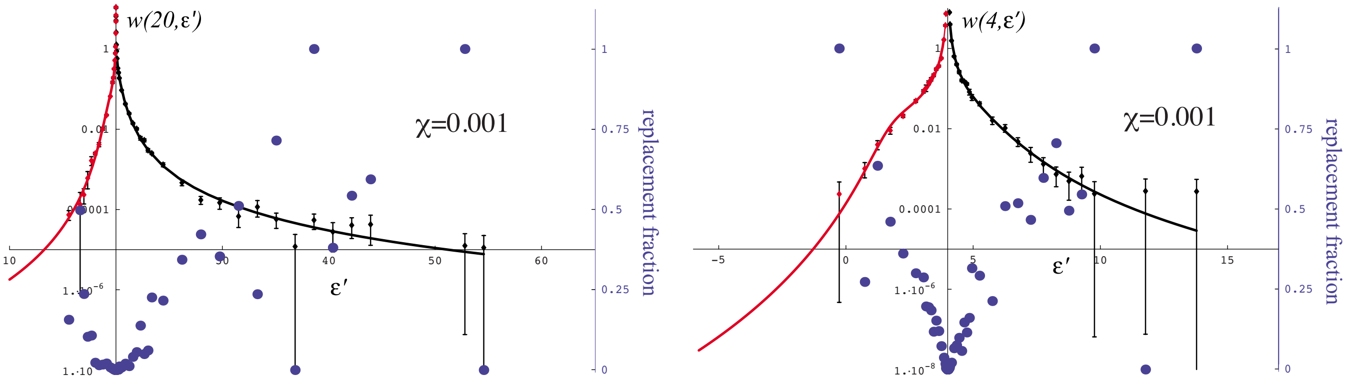

FIG. 5. (Color online) The transition probability rate densities $w(4,\epsilon')$ and $w(20,\epsilon')$ as extracted from the Monte-Carlo simulation for $\chi=0.001$. The lines represent fitting functions which are defined independently for the left and right sides of the distribution. A diffusive model is used to approximate the contribution to Eq. (23) from the region $-0.1<(\epsilon'-\epsilon)<0.1$, but a smoothed version of the fit is used for the rest of the integral. The large dots (right axis) indicate the fraction of collisions in each bin where the bound positron was liberated and replaced by the initially free positron.

The grid runs from 0.1 to 100 in ϵ and ϵ', with a spacing of 0.1. Variation along ϵ was smoothed by replacing each point with an average of itself and the point along the line connecting the two adjacent points corresponding to the same ϵ value, represented by the following algorithm:

$$w_{i,j}=\frac{1}{2}\left[w_{i,j}^{(0)}+w_{i-1,j}^{(0)}+\frac{w_{i+1,j}^{(0)}-w_{i-1,j}^{(0)}}{\epsilon_{i+1}-\epsilon_{i-1}}(\epsilon_i-\epsilon_{i-1})\right].$$

Above, the i and j indices represents ϵ and $\Delta\epsilon=\epsilon'-\epsilon$ variation, respectively. The values $w_{i,j}^{(0)}$ are the original, unsmoothed fitting functions with the singular point at $\epsilon=\epsilon'$ omitted. The algorithm was applied to every point but the endpoints. This procedure helps ensure a smoother, more physical time evolution of $f(\epsilon)$. Rapid, monotonic variation in $\Delta\epsilon$ precludes the need for smoothing in this parameter. Transitions near $\epsilon=\epsilon'$ were treated with a diffusive model (see below).

As a check on our numerics, we have tested where the

TABLE I. Three-body recombination rate coefficient C versus magnetization parameter χ. The fitting parameters for $w(\epsilon,\epsilon')$ [see Eq. (28)] at $\chi=0$ (infinite magnetic field). The left and right cutoffs are given by the functions $\Delta\epsilon_{\min}=-(1/2)[5.468\epsilon^{1.248}/(4.445+\epsilon^{1.248})+6.010\epsilon^{1.321}/(4.353+\epsilon^{1.321})]$ and $\Delta\epsilon_{\max}=(1/2)(0.777\epsilon^{1.049}+1.160\epsilon^{1.073})$. For $\epsilon<20$, the detailed balance form w_{db} [Eq. (31)] is used. Only the right fits are employed in this range.

	Left fit				Right fit				
ϵ	A_L	B_L	α_L	β_L	A_R	B_R	α_R	β_R	$D_{\delta\epsilon}$
0.1	0.1504	0.6056	23 540	2.502	0.1046	0.559	71 590	2.655	0.355 4
1	70.88	1.415	6673	12.29	15.25	1.131	698.7	2.395	0.044 67
2	47.03	1.265	66.65	5.064	52.52	1.296	267.9	2.871	0.010 9
3	76.52	1.431	0.3462	11.33	98.08	1.463	34.5	3.84	0.004 253
4	65.74	1.315	10.68	4.693	87.73	1.386	14.49	4.943	0.002 198
5	81.43	1.363	2.911	5.878	72.33	1.319	5.903	4.948	0.001 216
7	81.34	1.274	3.138	5.673	62.91	1.176	10.53	3.426	0.000 525 9
10	81.15	1.207	20.94	3.862	57.61	1.041	9.884	3.076	0.000 204 3
13	105.3	1.247	14.43	4.214	81.01	1.196	0.002 043	6.619	0.000 117 8
15	88.3	1.14	35.38	3.604	64.11	1.071	7.975	2.587	0.000 080 32
18	94.16	1.15	52.93	2.953	65.99	1.034	0.625	3.599	0.000 049 37
20	123	1.218	11.27	5.029	90.76	1.136	0.010 5	4.774	0.000 036 03
23	84.9	1.057	68.34	3.313	60.91	0.9181	3.651	2.752	0.000 023 59
25	146.7	1.265	26.19	3.613	69.14	0.9683	1.382	2.933	0.000 021 95
30	179.4	1.28	1.794	5.792	64.86	0.9684	1.915	2.719	0.000 013 04
40	80.43	0.9935	128.3	2.813	66.33	0.8854	5.307	2.311	7.144×10^{-6}
50	94.45	1.021	67.83	2.992	81.05	1.009	0.177	3.169	4.665×10^{-6}
60	106.3	1.026	67.06	3.665	73.96	0.9375	0.853 6	2.619	2.914×10^{-6}
70	127.4	1.03	38.07	4.158	69.58	0.9128	1.504	2.436	2.027×10^{-6}
80	148.7	1.095	26.43	4.599	82.75	0.9705	0.082 78	3.124	1.491×10^{-6}
90	105.4	0.9857	59.2	3.642	77.41	0.9405	0.456 2	2.617	1.327×10^{-6}
100	138	1.058	21.71	4.576	75.81	0.9044	0.271	2.825	9.751×10^{-7}

TABLE II. The fitting parameters for $w(\epsilon,\epsilon')$ [see Eq. (28)] at $\chi=0.001$. The left and right cutoffs are given by the functions $\Delta\epsilon_{\min}=-(1/2)\times[5.045\epsilon^{1.218}/(2.844+\epsilon^{1.218})+5.307\epsilon^{1.235}/(2.949+\epsilon^{1.235})]$ and $\Delta\epsilon_{\max}=(1/2)(1.182\epsilon^{1.083}+2.001\epsilon^{1.115})$. For $\epsilon<20$, the detailed balance form w_{db} [Eq. (31)] is used. Only the right fits are employed in this range.

	Left fit				Right fit				
ϵ	A_L	B_L	α_L	β_L	A_R	B_R	α_R	β_R	$D_{\delta\epsilon}$
0.1	4037	2.126	2.001×10^{10}	7.853	8853	2.203	8.415×10^{7}	5.158	0.3819
1	68.56	1.421	3607	10.51	54.41	1.369	717.5	2.767	0.047 8
2	79.39	1.539	3.315	10.61	77.72	1.424	214.1	3.375	0.011 63
3	67.69	1.45	6.606	6.499	72.71	1.446	74.48	3.359	0.007 069
4	86.72	1.68	0.090 73	9.453	91.26	1.707	10.42	4.351	0.007 572
5	87.12	1.938	2.43	5.527	90.23	1.974	1.349	4.879	0.009 146
7	92.19	2.398	0.016 02	9.16	55.3	2.166	1.843	3.892	0.009 197
10	0.4479	0.4127	54.47	3.078	0.4816	0.4709	24.08	2.689	0.004 058
13	1.838	0.7418	29.06	3.905	0.8423	0.4916	11.07	2.781	0.001 656
15	2.211	0.7622	20.41	4.053	1.56	0.6736	6.527	2.786	0.001 091
18	5.459	1.09	6.583	4.85	3.665	0.9685	2.645	3.05	0.000 665 8
20	5.832	1.043	6.205	4.351	2.277	0.7394	5.004	2.476	0.000 497 9
23	13.66	1.395	0.508 9	6.285	5.507	1.051	1.857	2.804	0.000 358 4
25	11.91	1.265	2.41	5.176	7.423	1.144	0.715 3	3.098	0.000 283 5
30	21.64	1.477	0.637 1	6.03	11.43	1.263	0.132 5	3.436	0.000 175 5
40	42.61	1.675	2.565	4.915	15.4	1.32	0.030 25	3.42	0.000 094 84
50	35.02	1.504	77.9	3.38	17.44	1.339	0.001 338	3.944	0.000 060 89
60	54.03	1.515	57.2	3.668	15.62	1.28	0.000 116 6	4.488	0.000 032 53
70	37.83	1.284	86.61	3.396	12.01	1.294	1.478×10^{-10}	7.454	0.000 026 55
80	30.61	1.144	15.31	4.476	11.74	1.236	0.002 453	3.457	0.000 016
90	14.39	0.9845	10.42	4.987	13.55	1.279	0.001 039	3.438	0.000 012 27
100	10.01	0.9653	5.311	5.08	14.31	1.32	0.000 429 2	3.628	0.000 010 96

function $w(\epsilon,\epsilon')$ obeys detailed balance. This requires the integrand in Eq. (23) to vanish when the distribution function takes the thermal equilibrium form $f_{\text{th}}(\epsilon)$:

$$f_{\text{th}}(\epsilon)w(\epsilon,\epsilon')=f_{\text{th}}(\epsilon')w(\epsilon',\epsilon). \tag{29}$$

For $v_\perp=0$ (and $T_\perp=0$), the thermal equilibrium density of particles in phase space is

$$P_{\text{th}}(\epsilon)=\frac{n}{(2\pi\bar{v}^2)^{1/2}}e^{\epsilon}.$$

This form neglects positron-positron interactions, equivalent to assuming $nb^3\ll1$. In this limit, the number density $f_{\text{th}}(\epsilon)$ is given by

$$f_{\text{th}}(\epsilon)=\zeta(\epsilon)P_{\text{th}}(\epsilon),$$

where $\zeta(\epsilon)$ is the density of states at energy ϵ. The value of $\zeta(\epsilon_0)$ is equivalent to the area of the phase-space surface defined by energy $\epsilon=\epsilon_0$:

$$\zeta(\epsilon_0)=4\pi\int\delta[\epsilon_{\text{GC}}(r,v_z)-\epsilon_0]r^2drdv_z.$$

Above, we use the guiding-center ($v_\perp=0$) expression for the energy appropriate for our simulation [Eq. (8)]. The integral can be performed analytically, and the result is

$$f_{\text{th}}(\epsilon)=\frac{5\pi^{3/2}}{4}nb^3\frac{e^{\epsilon}}{\epsilon^{7/2}}. \tag{30}$$

The fitting form used for $w(\epsilon,\epsilon')$ [Eq. (28)] is phenomenological and does not guarantee detailed balance. In Fig. 6, we compare the two sides of Eq. (29) for three values of the atomic binding energy ϵ to check detailed balance. The thermal equilibrium distribution function $f_{\text{th}}(\epsilon)$ used is the one appropriate for the guiding-center drift atom regime [Eq. (30)]. The figure shows that our measured transition rates satisfy detailed balance at shallow and moderate binding, but at deep binding there is a discrepancy. This is because we employed a two-temperature distribution for the positrons, taking $\mathbf{v}_\perp=0$. This is not important at shallow or moderate binding, but at deep binding, close collisions are more likely to cause energy exchange with the perpendicular degrees of freedom. As a result, transitions to deeper binding are somewhat more favored than detailed balance would predict, because the plasma is colder in the perpendicular degrees of freedom than is assumed by detailed balance.

To assure that detailed balance is exactly satisfied in the low-ϵ regime, we replace the fitting function in this

TABLE III. The fitting parameters for $w(\epsilon,\epsilon')$ [see Eq. (28)] at $\chi=0.005$. The left and right cutoffs are given by the functions $\Delta\epsilon_{\min}=-(1/2)\times[4.208\epsilon^{1.344}/(1.885+\epsilon^{1.344})+4.160\epsilon^{1.349}/(1.842+\epsilon^{1.349})]$ and $\Delta\epsilon_{\max}=(1/2)(2.668\epsilon^{1.240}+1.242\epsilon^{1.264})$. For $\epsilon<10$, the detailed balance form w_{db} [Eq. (31)] is used. Only the right fits are employed in this range.

	Left fit				Right fit				
ϵ	A_L	B_L	α_L	β_L	A_R	B_R	α_R	β_R	$D_{\delta\epsilon}$
0.1	1.06×10^{8}	5.88	2735.0	2.031	5.456	1.097	711 40.0	2.844	0.390 7
1	74.82	1.49	950.3	7.04	136.3	1.624	519.3	3.377	0.047 44
3	90.44	1.953	0.06559	11.5	134.8	2.12	0.730 2	6.487	0.022 37
5	54.22	2.101	4.352	5.705	27.01	1.848	11.23	3.333	0.015 64
7	7.026	1.266	37.06	3.569	6.965	1.29	8.924	3.039	0.006 272
10	19.73	1.541	2.69	5.838	13.05	1.391	1.467	3.38	0.001 981
12	21.24	1.451	4.195	5.236	17.43	1.44	0.352 1	3.63	0.001 106
15	55.4	1.711	0.2511	7.284	24.5	1.484	0.008 166	4.339	0.000 581 9
20	77.61	1.636	13.29	4.819	24.34	1.258	0.063 54	3.44	0.000 219 2
25	22.51	1.207	86.02	3.253	15.05	1.38	0.001 401	4.177	0.000 204 4
30	13.96	1.172	32.51	4.841	17.43	1.375	0.002 155	3.8	0.000 163
35	8.743	1.053	16.9	5.32	16.09	1.407	0.003 868	3.584	0.000 159 2
40	2.151	0.6582	37.17	4.065	15.19	1.57	0.000 048 56	4.233	0.000 137 9
50	1.09	0.4703	61.87	4.212	9.523	1.76	0.065 23	3.611×10^{-9}	0.000 096 4
60	0.4087	0.1642	58.77	3.458	8.247	1.678	0.063 9	5.399×10^{-11}	0.000 066 46
70	0.5294	0.1882	43.36	3.119	0.1172	4.028×10^{-9}	3.991	1.663	0.000 052 43
80	0.529	0.1931	50.44	3.368	9.45	1.464	9.435×10^{-6}	3.957	0.000 041 86
90	2.07	0.6824	27.06	3.557	9.227	1.41	0.000 098 37	3.373	0.000 034 73
100	3.856	0.9123	15.65	3.976	8.905	1.337	7.067×10^{-8}	4.665	0.000 028 48

range with an analytic form that automatically meets this condition:

$$w_{\mathrm{db}}(\epsilon,\epsilon')=\begin{cases}\dfrac{f_{\mathrm{th}}(\epsilon')}{f_{\mathrm{th}}(\epsilon)}w(\epsilon',\epsilon) & \text{for } \epsilon'<\epsilon\\ w(\epsilon,\epsilon') & \text{for } \epsilon'>\epsilon\end{cases}. \tag{31}$$

Here, $w(\epsilon,\epsilon')$ is the smoothed function described above. We use the detailed balance form w_{db} for $\epsilon<20$ for the $\chi=0$ and $\chi=0.001$ cases and for $\epsilon<10$ in the $\chi=0.005$ case. This adjustment assures the highest accuracy in the low-ϵ range where detailed balance is satisfied.

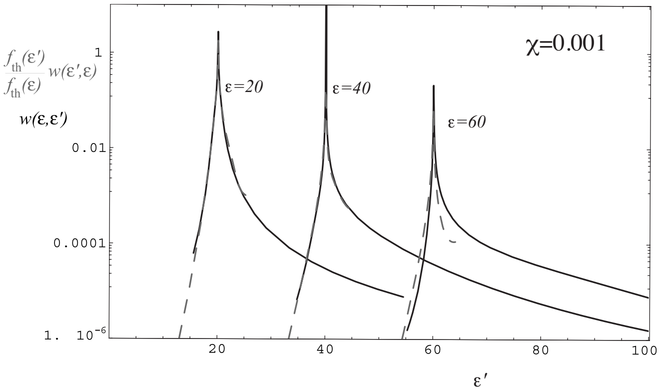

FIG. 6. A comparison of $[f_{\mathrm{th}}(\epsilon')/f_{\mathrm{th}}(\epsilon)]w(\epsilon',\epsilon)$ (gray, dashed lines) and $w(\epsilon,\epsilon')$ (black, solid lines) [rescaled forms of the first and second terms in Eq. (23) in thermal equilibrium] for three energies ϵ (20, 40, and 60) and plotted against ϵ', for $\chi=0.001$. Detailed balance requires the two terms to be equal. At large ϵ, detailed balance fails because the zero-temperature, perpendicular degrees of freedom participate in the collision in this range.

It is important to truncate the fit for $w(\epsilon,\epsilon')$ near the energy of the largest observed transition from the simulation, for both $\epsilon'>\epsilon$ and $\epsilon'<\epsilon$. Outside the range $\Delta\epsilon_{\min}<\epsilon'-\epsilon<\Delta\epsilon_{\max}$, $w(\epsilon,\epsilon')$ is set to zero. Expressions for $\Delta\epsilon_{\min}$ and $\Delta\epsilon_{\max}$ are given in the captions to Tables I–III. If the entire power-law tail in Fig. 5 is included, as many as 20 transition events are predicted to occur in the removed region for the simulated number of collisions. In fact, no transitions appear in this region, justifying the removal. The cutoff has a clear physical meaning for negative transitions. Jumps larger than $\epsilon'-\epsilon<1$ will be exponentially unlikely because a thermal positron cannot impart more than its kinetic energy to the atom. When detailed balance is satisfied, the cutoff for negative transitions implies one for positive transitions. Without such a cutoff, the expression for $w_{\mathrm{db}}(\epsilon,\epsilon')$ in Eq. (31) would diverge as $\epsilon'\rightarrow0$ where $f_{\mathrm{th}}(\epsilon')\rightarrow\infty$ [see Eq. (30)]. Our simulation results, which indicate that a single collision event cannot result in an arbitrarily large jump to deeper binding, verify the existence of this forward cutoff. Note that while truncation of $w(\epsilon,\epsilon')$ implies that deeply bound states are not populated after only one collision *event*, such states can still be populated within one collision *time* $(n\bar{v}b^2)^{-1}$, as a result of multiple collisional deexcitations. Truncation of the tail in $w(\epsilon,\epsilon')$ is further tested in the section on distribution evolution.

The fit used in Eq. (28) diverges at $\epsilon=\epsilon'$, so does not describe the central peak of $w(\epsilon,\epsilon')$ accurately. However, the small steps in energy accounted for in this narrow region can be treated with Fokker–Planck theory. The contribution to the integral in the master equation from the region

$-\delta\epsilon < (\epsilon' - \epsilon) < \delta\epsilon$ is approximated by expanding the first term in the integrand of Eq. (23).

To facilitate derivation of the Fokker–Planck equation, we define $\mathcal{W}(\epsilon, \Delta\epsilon) = w(\epsilon, \epsilon - \Delta\epsilon)$. Letting $\epsilon' = \epsilon + \Delta\epsilon$, we get

$$\begin{aligned}\int_{\epsilon-\delta\epsilon}^{\epsilon+\delta\epsilon} f(\epsilon')w(\epsilon',\epsilon)d\epsilon' &= \int_{-\delta\epsilon}^{\delta\epsilon} f(\epsilon+\Delta\epsilon)\mathcal{W}(\epsilon+\Delta\epsilon,\Delta\epsilon)d\Delta\epsilon \\ &\simeq \int_{-\delta\epsilon}^{\delta\epsilon}\left[f(\epsilon)\mathcal{W}(\epsilon,\Delta\epsilon) + \Delta\epsilon\frac{\partial}{\partial\epsilon}[f(\epsilon)\mathcal{W}(\epsilon,\Delta\epsilon)] \right. \\ &\quad \left. + \frac{1}{2}\Delta\epsilon^2\frac{\partial^2}{\partial\epsilon^2}[f(\epsilon)\mathcal{W}(\epsilon,\Delta\epsilon)]\right]d\Delta\epsilon. \end{aligned} \tag{32}$$

Reverting to notation in terms of $w(\epsilon, \epsilon')$, substitution of Eq. (32) into Eq. (23) gives

$$\begin{aligned}\frac{\partial f}{\partial t} &= \int_{-\infty}^{\epsilon-\delta\epsilon}[f(\epsilon')w(\epsilon',\epsilon) - f(\epsilon)w(\epsilon,\epsilon')]d\epsilon' \\ &\quad - \frac{\partial}{\partial\epsilon}\left[M_{\delta\epsilon}(\epsilon)f(\epsilon) - D_{\delta\epsilon}(\epsilon)\frac{\partial f}{\partial\epsilon}\right] \\ &\quad + \int_{\epsilon+\delta\epsilon}^{\infty}[f(\epsilon')w(\epsilon',\epsilon) - f(\epsilon)w(\epsilon,\epsilon')]d\epsilon', \end{aligned} \tag{33}$$

where the diffusion coefficient $D_{\delta\epsilon}(\epsilon)$ and mobility coefficient $M_{\delta\epsilon}(\epsilon)$ are defined as

$$D_{\delta\epsilon}(\epsilon) \equiv \frac{1}{2}\int_{\epsilon-\delta\epsilon}^{\epsilon+\delta\epsilon}(\epsilon' - \epsilon)^2 w(\epsilon,\epsilon')d\epsilon', \tag{34}$$

$$M_{\delta\epsilon}(\epsilon) \equiv \int_{\epsilon-\delta\epsilon}^{\epsilon+\delta\epsilon}(\epsilon' - \epsilon)w(\epsilon,\epsilon')d\epsilon' + \frac{\partial}{\partial\epsilon}D_{\delta\epsilon}(\epsilon). \tag{35}$$

In thermal equilibrium, the condition of detailed balance requires

$$M_{\delta\epsilon}(\epsilon)f_{\text{th}}(\epsilon) - D_{\delta\epsilon}(\epsilon)\frac{\partial f_{\text{th}}(\epsilon)}{\partial\epsilon} = 0.$$

The resulting Einstein relation for $M_{\delta\epsilon}$ and $D_{\delta\epsilon}$ is

$$M_{\delta\epsilon}(\epsilon) = D_{\delta\epsilon}(\epsilon)\frac{\partial f_{\text{th}}/\partial\epsilon}{f_{\text{th}}(\epsilon)}. \tag{36}$$

Either $D_{\delta\epsilon}$ or $M_{\delta\epsilon}$ can be extracted from the discrete simulation output, with the integral in Eqs. (35) and (36) being replaced by a sum over points in the range. However, since $M_{\delta\epsilon}$ involves a first moment of $w(\epsilon, \epsilon')$ as well as a derivative of $D_{\delta\epsilon}$ (which itself is defined only at discrete ϵ), we choose to use the Einstein relation for $M_{\delta\epsilon}$. While detailed balance does not hold for deeply bound atoms, it does for more weakly bound guiding-center atoms. Given the discrete simulation data, the $M_{\delta\epsilon}$ generated by Eq. (36) varies much more smoothly than its counterpart determined by Eq. (35).

VI. THEORY OF LARGE IMPACT PARAMETER COLLISIONS

Here we test the results of our simulation against a Fokker–Planck theory for collisions with large impact parameter. In the drift approximation, we develop a theoretical expression for the collision induced diffusion coefficient D_ϵ (distinct from $D_{\delta\epsilon}$) in the otherwise conserved energy ϵ. From an Einstein relation, we predict the first moment of $w(\epsilon, \epsilon')$ when only these large impact parameter collisions are considered. Good agreement is found at small to moderate binding energies ϵ, where guiding-center drift theory is applicable.

The development below follows Ref. 7, but includes the effect of z-axis bounce motion and preserves the diffusive term in the Fokker–Planck equation. Both effects decrease the energy-loss rate: the parallel degree of freedom picks up kinetic energy on adiabatic steps inward, reducing the net change in binding energy, and the diffusive term creates some flux away from the nucleus, resulting in a net decrease in energy-loss rate. In the analysis, collisions are assumed adiabatic in both z-axis and cyclotron dynamics. If the collision duration is much greater than one parallel bounce period, guiding-center atom frequency ordering implies that it is also much longer than a cyclotron period:

$$\frac{\rho_{\min}}{\bar{v}} \gg \omega_z^{-1} \gg \Omega_c^{-1}. \tag{37}$$

Here, $\rho_{\min}$ is the minimum impact parameter considered. The assumption always holds for sufficiently large choice of $\rho_{\min}$.

Within the atom, cylindrical symmetry about the magnetic field implies conservation of momentum p_ϕ. In a collision, p_ϕ can change, but I_z and μ are still assumed static. For an ensemble of guiding-center atoms with distribution $f(I_z, p_\phi, \mu)$, the adiabatic invariance of I_z and μ means that all energy change is due to changes in p_ϕ. The flux in energy space is

$$\Gamma_\epsilon = M_\epsilon f - D_\epsilon\frac{\partial f}{\partial\epsilon}. \tag{38}$$

Here, D_ϵ is the diffusion coefficient in coordinate ϵ and M_ϵ is the energy-space mobility. The mobility is related to the diffusion coefficient by an Einstein relation of the form of Eq. (36). Note that in the previous analysis, $D_{\delta\epsilon}$ and $M_{\delta\epsilon}$ were determined for energy steps smaller than $\delta\epsilon$. Here, we are instead considering collisions with an impact parameter larger than $\rho_{\min}$.

The diffusion coefficient D_ϵ due to large impact parameter collisions is defined as

$$D_\epsilon = \tfrac{1}{2}\langle\nu\Delta\epsilon^2\rangle. \tag{39}$$

Here, $\Delta\epsilon$ is the change in energy experienced in the collision. The average is over initial conditions with collisional impact parameters greater than $\rho_{\min}$ and all atoms at fixed binding energy ϵ. The average over atomic variables is required to make D_ϵ a function of energy only, in keeping with a description of evolution in only this parameter. As before, if the distribution is a function of energy only, ergodically spread over phase space on each energy surface, then this description is self-consistent. The diffusion coefficient d_ϵ before the atom average is a function of both binding energy and atomic angular momentum. Once d_ϵ is found, we will average over atomic states to obtain D_ϵ. For colliding positrons streaming along the magnetic field lines at velocity v_z and intersecting the $z=0$ plane at position $\boldsymbol{\rho}_p$:

$$d_\epsilon = \frac{1}{2}\int_{-\infty}^{\infty} |v_z| e^{-v_z^2/2\bar{v}^2} \frac{n}{\sqrt{2\pi}\bar{v}} \Delta\epsilon^2 d^2\rho_p dv_z. \tag{40}$$

Only energy changes due to angular momentum changes are significant, so

$$\Delta\epsilon \approx \frac{\partial\epsilon}{\partial p_\phi}\Delta p_\phi = -\hat{\omega}_\phi \Delta\hat{p}_\phi. \tag{41}$$

In the guiding-center drift approximation, we may discard the kinetic piece in the canonical angular momentum p_ϕ from Eq. (6). In this limit, a step in p_ϕ is equivalent to a step along cylindrical radius ρ:

$$\Delta p_\phi \approx m_e \Omega_c \rho \Delta\rho. \tag{42}$$

As long as the bounce frequency ω_z is much faster than the drift frequency ω_ϕ, the drift orbit can be considered of uniform speed. If the impact parameter ρ_p is also much larger than $1/\epsilon$, the atomic length scale, we may use (from Ref. 7)

$$\Delta\rho = -2\chi b^2 \bar{v} \sin(\phi) \left|\frac{\omega_\phi}{v_z^2}\right| K_1\left(\left|\frac{\omega_\phi \rho_p}{v_z}\right|\right). \tag{43}$$

This is the radial step taken in one collision, where ϕ is the relative angle between the bound and passing positrons' position vectors at the moment when the passing positron crosses the $z=0$ plane. K_1 is the modified Bessel function of the first kind. Combining Eqs. (40)–(43) gives the diffusion coefficient d_ϵ in the $\mathbf{E}\times\mathbf{B}$ drift approximation:

$$d_\epsilon = 2\sqrt{2\pi}(n\bar{v}b^2)\chi \hat{p}_\phi \hat{\omega}_\phi^2 \mathcal{F}\left(\frac{\omega_\phi \rho_{\min}}{\bar{v}}\right), \tag{44}$$

with

$$\mathcal{F}(\xi) \equiv \int_\xi^\infty \int_{-\infty}^{\infty} s K_1^2\left(\frac{s}{|x|}\right) \frac{e^{-x^2/2}}{|x|^3} dx ds. \tag{45}$$

This expression is valid in the guiding-center atom regime, defined as $\epsilon < \epsilon_c = \chi^{-2/3}$, for collisions with large parameter, and thus small individual steps in energy, only.

Lastly, we average d_ϵ from Eq. (44) over all available atom states at energy ϵ_0 to obtain the diffusion coefficient D_ϵ as a function of energy only. For simplicity of notation, let us introduce a dimensionless form of the diffusion coefficient $\hat{D}_\epsilon$:

$$\hat{D}_\epsilon = \frac{D_\epsilon}{(n\bar{v}b^2)}.$$

Then,

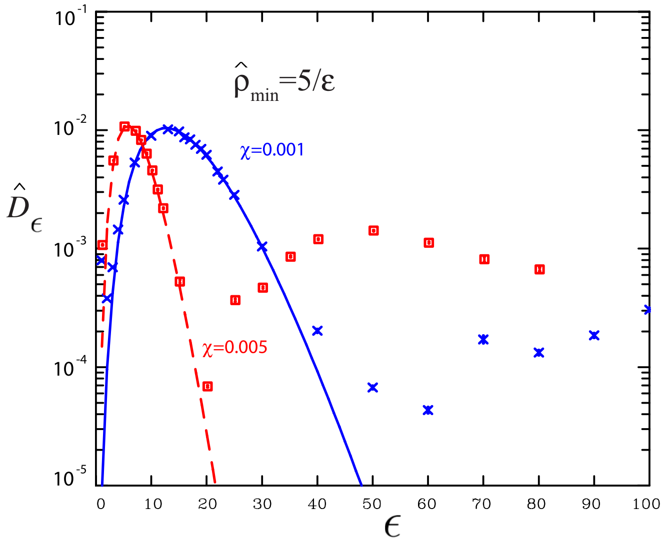

FIG. 7. (Color online) Theory (solid and dashed lines) and simulation (crosses and squares) for the diffusion coefficient $\hat{D}_\epsilon$ from collisions with impact parameter greater than $\hat{\rho}_{\min}=5/\epsilon$ at $\chi=0.001$ and $\chi=0.005$, respectively. The theory assumes guiding-center drift motion with adiabatic invariance of I_z. At deep binding energies ϵ, the $\mathbf{E}\times\mathbf{B}$ drift approximation becomes invalid as the atom passes into the chaotic regime and the theory fails.

$$\hat{D}_\epsilon = \frac{\int d_\epsilon \delta(\epsilon-\epsilon_0) dp_\phi dI_z}{n\bar{v}b^2 \int \delta(\epsilon-\epsilon_0) dp_\phi dI_z},$$

$$\hat{D}_\epsilon = 2\sqrt{2\pi}\chi \frac{\displaystyle\int \hat{p}_\phi \frac{\hat{\omega}_\phi^2}{\hat{\omega}_z} \mathcal{F}\left(\frac{\omega_\phi \rho_{\min}}{\bar{v}}\right) dp_\phi}{\displaystyle\int \frac{1}{\hat{\omega}_z} dp_\phi}. \tag{46}$$

We may extract the diffusion coefficient $\hat{D}_\epsilon$ from the simulation results as well. Recalling that the final distribution in the simulation is proportional to $w(\epsilon,\epsilon')$, we can use Eq. (34), letting $w(\epsilon,\epsilon')$ be the appropriately weighted distribution from only those collisions with impact parameter above $\rho_{\min}$ and extending $\delta\epsilon$ to ∞. The integral becomes the following discrete sum:

$$\hat{D}_\epsilon = \frac{1}{2}\sqrt{2\pi}\left[\left(\frac{10}{\epsilon}\right)^2 - \hat{\rho}_{\min}^2\right] \frac{1}{N}\sum_{i=1}^{N} (\Delta\epsilon_i)^2. \tag{47}$$

The impact parameters considered for purposes of calculating $\hat{D}_\epsilon$ lie in the range from $\hat{\rho}_{\min} < \hat{\rho}_p < 10/\epsilon$. Since the simulation samples all possible atom initial conditions at a fixed binding energy as well, the average over all accessible atomic states (for a given ϵ) is included in the sum above.

In Fig. 7, simulation and theory for $\hat{D}_\epsilon$ agree over a range of binding energies before the chaotic cutoff. As binding energy increases, ω_ϕ increases and eventually exceeds the inverse collision duration $\bar{v}/\rho_{\min}$. An exponential decrease in $\hat{D}_\epsilon$ is observed as p_ϕ becomes adiabatically invariant on the collision timescale. At deep binding, cyclotron motion becomes relevant and the theory expression (46), derived using the $\mathbf{E}\times\mathbf{B}$ drift approximation, no longer applies.

The adiabatic invariance of I_z is confirmed *a posteriori* by agreement between theory and simulation at midrange energies.

We now calculate the mean rate at which energy is lost by an ensemble of guiding-center atoms at an initial binding energy ϵ due to diffusion and mobility caused by large impact parameter collisions. We will use the Fokker–Planck flux in ϵ of Eq. (38) and the theoretical expression for $\hat{D}_\epsilon$ in Eq. (46).

Consider an ensemble $f(\epsilon)$ of atoms distributed in energy ϵ. The average binding energy ϵ is

$$\bar{\epsilon} = \frac{\int \epsilon' f(\epsilon') d\epsilon'}{\int f(\epsilon') d\epsilon'}. \tag{48}$$

The energy-loss rate follows:

$$\frac{\partial \bar{\epsilon}}{\partial t} = \frac{\displaystyle\int \epsilon' \frac{\partial f}{\partial t} d\epsilon'}{\displaystyle\int f(\epsilon') d\epsilon'}. \tag{49}$$

The continuity equation

$$\frac{\partial f}{\partial t} = -\frac{\partial \Gamma_{\epsilon'}}{\partial \epsilon'}, \tag{50}$$

combined with Eq. (39), closes the system. Choosing $f(\epsilon') = \delta(\epsilon' - \epsilon)$ gives the energy-loss rate $\partial \bar{\epsilon}/\partial t|_{\text{drag}}$ due to large impact parameter collisions at energy ϵ. Integrating by parts twice:

$$\left.\frac{\partial \bar{\epsilon}}{\partial t}\right|_{\text{drag}} = \int \left(M_\epsilon + \frac{\partial D_\epsilon}{\partial \epsilon'} \right) \delta(\epsilon' - \epsilon) d\epsilon' .$$

The Einstein relation (36) gives the mobility coefficient M_ϵ. In our dimensionless variables, the energy-loss rate due to drag is

$$\left.\frac{\partial \bar{\epsilon}}{\partial \tau}\right|_{\text{drag}} = \hat{D}_\epsilon \frac{\partial f_{\text{th}}/\partial \epsilon}{f_{\text{th}}(\epsilon)} + \frac{\partial \hat{D}_\epsilon}{\partial \epsilon}, \tag{51}$$

where $\tau = n\bar{v}b^2 t$.

The first term in the numerator of Eq. (51) arose from the first term in Eq. (38), and thus represents energy loss due to mobility flux. This term is positive definite beyond the kinetic bottleneck, as one would expect. The second term arises from the second term in Eq. (38), representing change in binding energy due to diffusive spreading. The second, diffusive term can be positive or negative, as seen in Fig. 7.

A procedure similar to that leading to Eq. (47) gives $\partial \bar{\epsilon}/\partial \tau|_{\text{drag}}$ from the simulation. This time we calculate the first moment of $w(\epsilon, \epsilon')$:

$$\frac{\partial \epsilon}{\partial \tau} = \sqrt{2\pi} \left[\left(\frac{10}{\epsilon} \right)^2 - \hat{\rho}_{\min}^2 \right] \frac{1}{N} \sum_{i=1}^{N} \Delta \epsilon_i . \tag{52}$$

Again, only collisions beyond radius $\hat{\rho}_{\min}$ and within radius $10/\epsilon$, the maximum considered in the simulation, are considered in the sum.

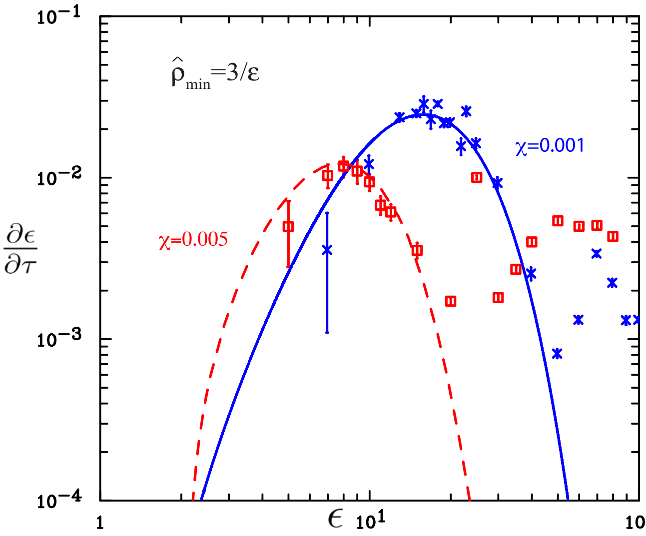

FIG. 8. (Color online) The energy-loss rate due to large impact parameter collisions ($\hat{\rho}_{\min} = 3/\epsilon$) for $\chi = 0.001$ (crosses) and $\chi = 0.005$ (squares). The theory lines come from Eq. (51). The exponential cutoff at large ϵ is observed in the simulation results until the chaotic cutoff energy is approached ($\epsilon_c = 100$ and $\epsilon_c = 34.2$ for $\chi = 0.001$ and $\chi = 0.005$, respectively), after which the drift approximation used in deriving the transport coefficient D_ϵ is invalid.

Equations (51) and (52) give the mean energy-loss rate due to collisions outside the cutoff radius $\rho_{\min}$ as a function of the binding energy ϵ. The minimum impact parameter $\rho_{\min}$ can be chosen arbitrarily, as long as it satisfies $\hat{r}_{\min} \gg \epsilon^{-1}$. Figure 8 shows the energy-loss rate from Eq. (51) compared with the same rate obtained from the Monte-Carlo simulation. As ϵ increases, the loss rate also increases, up to $\epsilon \gtrsim \chi^{-1/2}$, at which point the adiabatic cutoff causes an order of magnitude reduction in the rate, as expected from guiding-center theory. This peak corresponds roughly to the energy at which the drift velocity equals the thermal velocity,

$$v_{\text{drift}} = \omega_\phi \frac{b}{\epsilon} \approx \bar{v} \chi \epsilon^2 = \bar{v}^2,$$

which occurs when

$$\epsilon = \chi^{-1/2}. \tag{53}$$

At larger energies, where $\epsilon \lesssim \chi^{-2/3}$, the atom enters the chaotic regime where guiding-center theory no longer applies. For $\epsilon \approx \chi^{-2/3}$, the timescale of rotational motion of the positron about the antiproton is set by the cyclotron frequency and is roughly independent of ϵ. At still larger values of ϵ, i.e., $\epsilon \gg \chi^{-2/3}$, the atom becomes effectively unmagnetized and we would again expect a reduction in the loss rate with increasing ϵ. However, we have not studied this unmagnetized regime in detail. For $\chi = 0.001$, it would require $\epsilon \gg 100$.

Figure 9 shows the energy-loss rate due to all collisions. The simulation gives the contribution from impact parameters $\hat{\rho}$ below $10/\epsilon$ [through Eq. (52) with $\rho_{\min} = 0$]. The theory gives the (small) contribution for all larger impact parameters. For the infinite-magnetic-field ($\chi = 0$) case, ϵ scaling comes from dimensional arguments:[4]

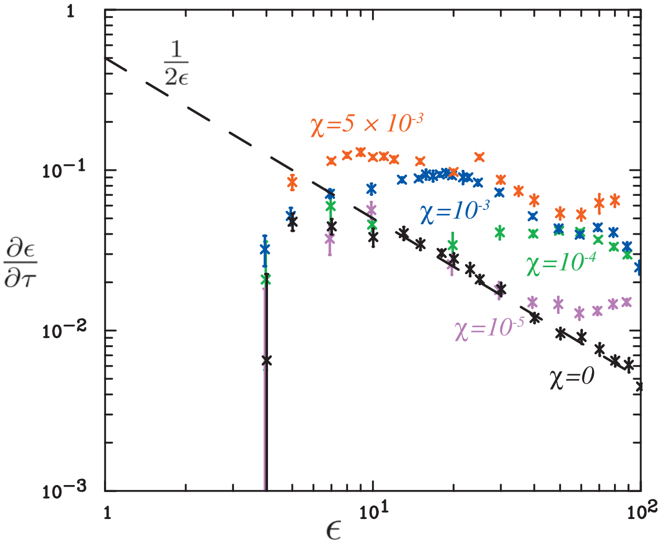

FIG. 9. (Color) The total collisional energy-loss rate for $\chi=0$, 10^{-5}, 10^{-4}, 10^{-3}, and 5×10^{-3}.

$$\lim_{\chi\to 0}\frac{\partial\epsilon}{\partial\tau}\simeq\frac{1}{2\epsilon}. \tag{54}$$

This is merely a statement that the collisional cross section scales roughly as $1/\epsilon^2$. However, when the field is finite, energy loss from collisions with large impact parameter remains relevant even at deep binding (as seen in Fig. 8). In this case, the total collisional energy-loss rate does not drop as rapidly with binding energy. For the smaller values of χ, the energy-loss rate follows the infinite field form but deviates as ϵ approaches $\chi^{-1/2}$, as expected from Eq. (53). At this energy, drag on $\mathbf{E}\times\mathbf{B}$ drift motion is significant and the energy-loss rate is enhanced.

VII. DISTRIBUTION EVOLUTION

To calculate the rate of antihydrogen formation from a thermal plasma, we follow a method similar to that used by Glinsky and O'Neil in Ref. 4, assuming a thermal distribution of atoms at small binding energies ϵ. Unlike previous work, however, we use the master equation (23) directly, with only the transition probability rate density $w(\epsilon,\epsilon')$ derived from simulation. Once $w(\epsilon,\epsilon')$ has been established, this method allows us to rapidly predict the evolution of an arbitrary distribution of atomic energies. Each energy surface is assumed to remain uniformly populated during the evolution so that the distribution is a function of energy only. With such a simplification, there is a risk of discarding important dynamics. However, good agreement is found between predictions made with our method and a much more time-consuming method which follows many atoms through collisional evolution. We also find that our method predicts three-body recombination rates in agreement with previous work.[4,5]

In solving the master equation (33), we use a discrete grid with a spacing of $\delta\epsilon=0.1$ in ϵ, and omit the grid point associated with $\epsilon-\epsilon'=0$, since this point is accounted for through the terms proportional to $M_{\delta\epsilon}$ and $D_{\delta\epsilon}$. The time integration is performed using an adaptive-time-step, fourth-order explicit Runge–Kutta algorithm. To check the accuracy of this procedure, we compared it to a numerical simulation in which we followed an ensemble of 14 358 atoms through 100 collision times, preserving atom variables between collisions. Figure 10 shows good agreement between the simulation results and the solution of the master equation for an initial Gaussian distribution. The best agreement is found in the case where the cutoff $\Delta\epsilon$ in $w(\epsilon,\epsilon')$ is placed between the first empty bin and the largest observed transition (solid lines in Fig. 10). We therefore use this $\Delta\epsilon$ in the following numerical solution to the master equation (see captions to Tables I–III).

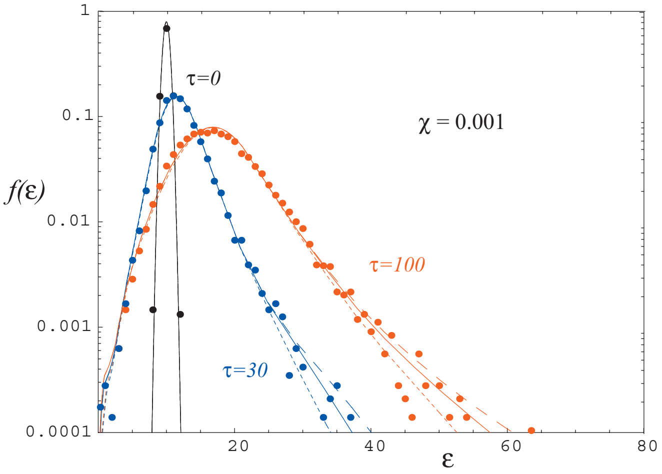

FIG. 10. (Color) The evolution of a sample Gaussian distribution centered at $\epsilon=10$ for $\chi=0.001$. The black curve shows the initial distribution, blue is after 30 collision times, and red is after 100 collision times. The three curves show the solution for different choices of the cutoff $\Delta\epsilon$ in $w(\epsilon,\epsilon')$. The cutoff was chosen either at the largest observed transition (dashed line), the first empty bin (dotted line), or an average of the two (solid line). The solid circles show the evolution of an ensemble of atoms that were chosen from the same initial distribution and followed through multiple collisions for the same amount of time. Best agreement is found for the solid line, so the middle value of $\Delta\epsilon$ is used in the simulation.

To predict the rate of antihydrogen formation, we set the initial distribution $f(\epsilon)=f_{\text{th}}(\epsilon)$ [from Eq. (30)] for $\epsilon<1$ and hold it fixed in this region. Maximum atom size and available states diverge at $\epsilon=0$. We truncate $f(\epsilon)$ at small ϵ by omitting the $\epsilon=0$ grid point. For $\epsilon>1$, $f(\epsilon)$ is initially zero and evolves according to the master equation. Deeper binding states become populated as atoms "trickle in" from the fixed thermal region. With this boundary condition, f is normalized such that the integral of f over all positive binding energies yields the total number of bound atoms per antiproton. Figure 11 shows the distribution $f(\epsilon)$ for various numbers of collision times with the magnetization parameters $\chi=0$ (infinite magnetic field), $\chi=0.001$, and $\chi=0.005$.

A roughly power-law distribution is established at deep binding, behind which a steady state is established. This power-law distribution moves to progressively deeper binding as time increases. The exponent in the power law decreases as χ increases, from roughly 8 at $\chi=0$ to roughly 5.5 at $\chi=0.005$, indicating that a weaker magnetic field allows more rapid population of deeply bound states. The value of 8

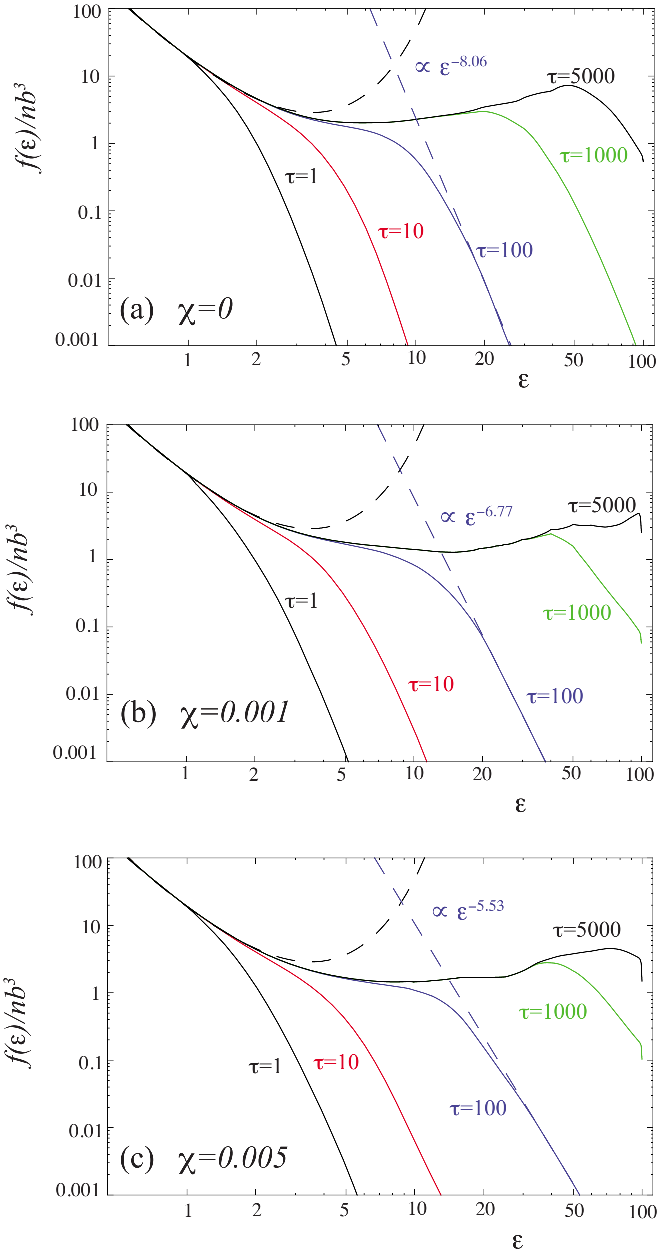

FIG. 11. (Color online) The distribution of antihydrogen atoms $f(\epsilon)$ for (a) $\chi=0$, (b) $\chi=0.001$, and (c) $\chi=0.005$ at $\tau=tn\bar{v}b^2=1$, 10, 100, 1000, and 5000. At deeper binding, the steady-state distribution takes longer to establish. The chaotic cutoff energies $\epsilon_c=\infty$, 100, and 34.2 for $\chi=0$, 0.001, and 0.005, respectively. The dashed curve indicates a thermal equilibrium distribution. The straight dashed lines are power-law fits to the tail region at $\tau=100$.

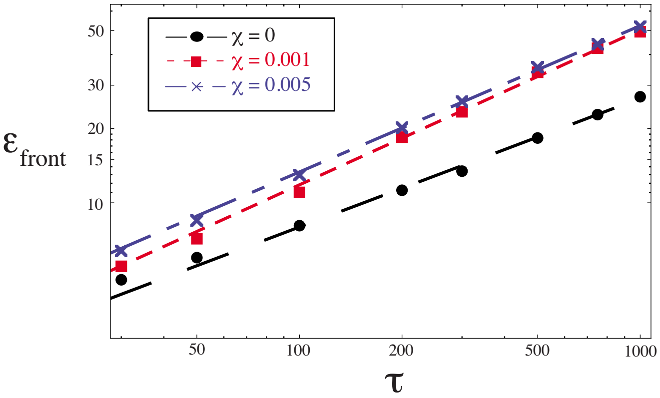

FIG. 12. (Color online) Location of the power-law tail as a function of time for three different values of χ (dots, squares, and crosses), together with fits (lines).

for the exponent for $\chi=0$ was also observed in the simulations of Glinsky and O'Neil.[4,12]

The rate at which the power-law tail moves to deeper binding is displayed in Fig. 12. This plot shows the time τ for which $f(\epsilon)$ at a given ϵ reaches half its steady-state value. The dashed lines are fits to the data, scaling as $\tau^{0.52}$ for $\chi=0$, $\tau^{0.63}$ for $\chi=0.001$, and $\tau^{0.59}$ for $\chi=0.005$. A scaling of $\epsilon \propto \tau^{1/2}$ for the front location is consistent with Eq. (54), and was also observed for $\chi=0$ by Glinsky and O'Neil.[4]

Figure 11 also shows that, as time increases, a steady-state (not thermal equilibrium) form for $f(\epsilon)$ is reached at progressively higher values of ϵ. In the steady-state region, a balance is reached where flux to deeper binding is independent of binding energy (divergence free). In thermal equilibrium, detailed balance means the net particle flux vanishes. Our steady state exists indefinitely only because the $f(\epsilon)=0$ boundary condition at $\epsilon=100$ provides an infinite sink of particle flux. In a physical system, the steady state becomes established from low energies down to the ground state, then the thermal distribution is populated from the ground state upward.

The time scale for the downward, steady-state flux is set by the collision frequency $n\bar{v}b^2$ [see Eq. (28)], while the number of thermal atoms available [Eq. (30)] scales with the small parameter nb^3. As previously predicted,[3–5] this constant flux R_3, the three-body recombination rate, must therefore be given by

$$R_3 = C(n\bar{v}b^2)(nb^3) \propto T^{-9/2}, \tag{55}$$

where the $T^{-9/2}$ scaling neglects the relatively weak dependence on T of the rate coefficient $C(\chi)$. This coefficient is given in Table IV for each value of χ simulated. These values are consistent with fluxes calculated previously for recombination in strong magnetic fields;[4,5] for instance, see Eq. (1). A stronger magnetic field (lower χ) inhibits flux through the kinetic bottleneck.

At deep binding the steady state takes many collision times to become established. Flux at binding energies ϵ greater than the maximum for which steady state has been established (for a given τ) does not have the simple temperature scaling of Eq. (55). Figure 13 shows the number of atoms that have reached binding energy ϵ, or larger, after 1, 10, 100, and 1000 collision times. Figure 14 shows this same quantity, but for a constant relaxation time t and binding energy U and varying temperature. Neither the number of

TABLE IV. Three-body recombination rate coefficient C versus magnetization parameter χ.

χ	0	0.001	0.005
C	0.076	0.10	0.14

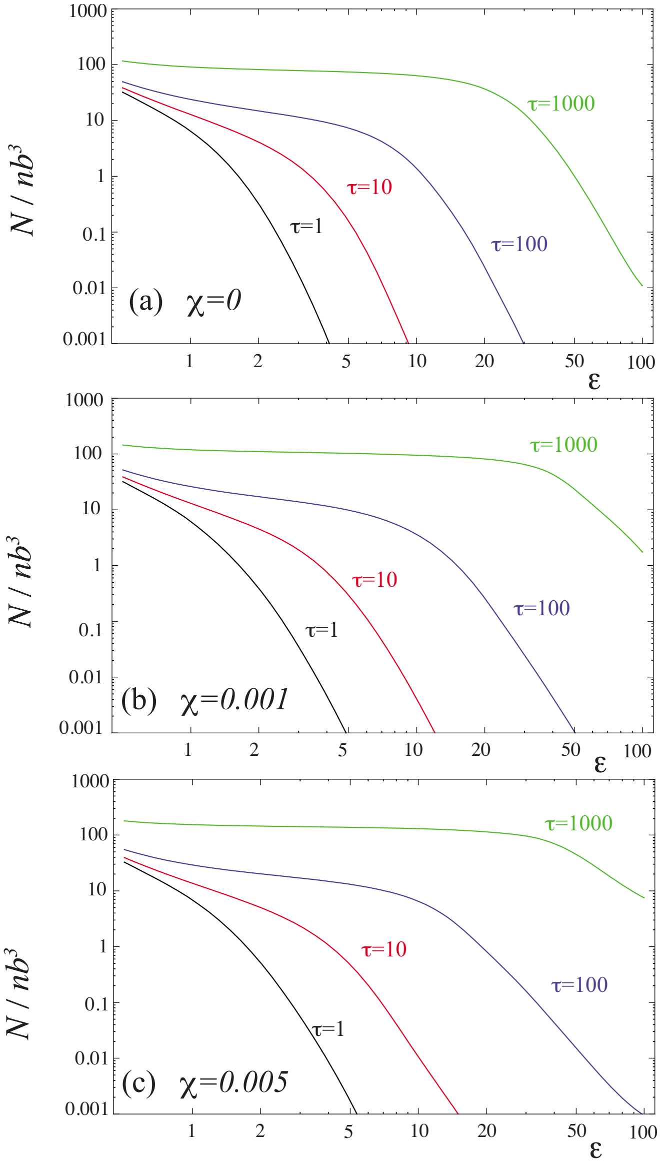

FIG. 13. (Color online) The number N of atoms per antiproton that have passed binding energy ϵ for (a) $\chi=0$, (b) $\chi=0.001$, and (c) $\chi=0.005$ for different numbers of collision times $\tau=tn\bar{v}b^2$. Note that N is scaled to nb^3, with $nb^3 \ll 1$ assumed.

collision times τ nor the rescaled binding energy ϵ are constant in this case. The $T^{-9/2}$ temperature scaling is only seen for long relaxation times, when the steady state has had time to become established.

In actual experiments, nearly all atoms exit the plasma in much less than the time required for a steady state distribution to be established at deep binding. Atomic state diagnostics in the ATRAP experiment show a field ionization spectrum equivalent to $f(\epsilon) \propto \epsilon^{-5}$.[6] This is consistent with our results at early times. In particular, the $\chi=0.005$ case shows a similar scaling for the power-law tail to that observed in the experiment (see Fig. 11).

At high temperatures, the fixed binding energy U is smaller than the kinetic bottleneck energy $4T$. For the choice of U in Fig. 14, i.e., $U=6.89$ meV$=80$ K, this occurs when $T>20$ K. In this temperature range the fraction N of atoms per antiproton depends much less strongly on the amount of time the antiproton spends in the trap, as shown by the convergence of the three curves in Fig. 14(a). In addition, for small relaxation times, the recombination fraction actually scales favorably with increasing temperature. Similar temperature scaling was predicted by Driscoll[12] based on results from Ref. 4.

Below the chaotic cutoff energy ϵ_c, we will show that radiation becomes more significant, dominating the cascade process. Once an atom is in the chaotic orbit regime, we will see that it relaxes to deep binding on its own through radiation much more rapidly than in the guiding-center drift regime.

VIII. RADIATION

In this section, we estimate the recombination rate due to electromagnetic radiation, using the classical Larmor formula,[9]

$$\frac{\partial U}{\partial t} = \frac{2}{3}\frac{e^2}{c^3}\ddot{\mathbf{x}} \cdot \ddot{\mathbf{x}}, \tag{56}$$

where U is the unscaled binding energy, given by Eq. (5).

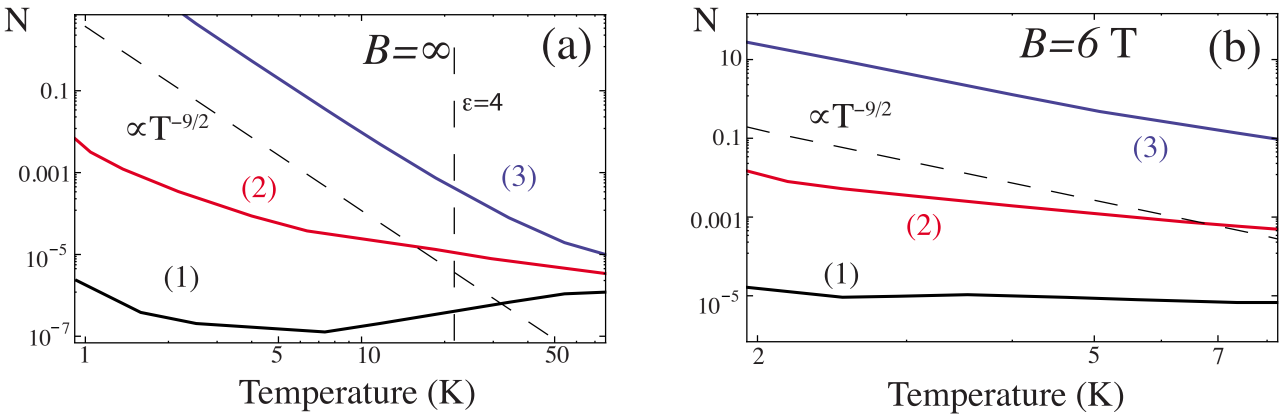

FIG. 14. (Color online) The fraction of atoms N, per antiproton, that have passed binding energy $U=6.89$ meV ($\epsilon=20$ at $T=4$ K), given 1.84 μs [curves labelled (1)], 7.36 μs [curves labelled (2)], and 184 μs [curves labelled (3)]. Density is fixed at 10^8 cm^{-3}. The times correspond to 25, 100, and 2500 collision times, respectively, given this density and a plasma temperature of 4 K. In (a), the magnetic field is infinite, so $\chi=0$ at all temperatures. In (b), $B=6$ T and χ ranges up to 0.005. The N shown is calculated from a linear interpolation between the discrete values of χ treated in the simulation.

Our procedure will be to calculate the energy-loss rate of a bound positron using this formula, assuming classical dynamics as in the previous sections. In addition, to simplify the analysis, we average the energy-loss rate over an ensemble of atoms described by ergodic distributions, as described below. We find that atoms in low-angular-momentum states radiate most rapidly, as the positrons in these atoms are able to strongly interact with the central antiproton. For such atoms, quantum effects neglected in our classical approach become important when p_ϕ is on the order of $\hbar$. We attempt to estimate the magnitude of these quantum effects on the radiative energy-loss rate, and find they are most important for weakly bound atoms in helical states, but less important for atoms near the chaotic regime where our classical estimates should be more relevant.

In what follows, we evaluate Eq. (56) in cylindrical coordinates, writing

$$U=\frac{e^2}{(\rho^2+z^2)^{1/2}}-\frac{1}{2m_e}\left[p_\rho^2+p_z^2+\left(\frac{p_\phi}{\rho}-\frac{1}{2}m_e\rho\Omega_c\right)^2\right], \tag{57}$$

where ρ is the cylindrical radius and ϕ the azimuthal angle, so that we may express the radiation rate in terms of the conserved quantities in the absence of radiation: p_ϕ and U. If the positron orbit is chaotic, these are the only constants of its motion. For an ergodic orbit, the time-average rate of change of U is equivalent to a phase-space average of $\partial U/\partial t$ at fixed U and p_ϕ, provided the radiation rate is sufficiently slow; that is, we assume

$$\frac{\dot{U}}{U},\frac{\dot{p}_\phi}{p_\phi}\ll\frac{\dot{\alpha}}{\alpha}, \tag{58}$$

where α is any phase-space variable except for p_ϕ. We also assume the α variables ergodically cover the available states. Even without the restriction in Eq. (58), the phase-space average of $\partial U/\partial t$ can be interpreted as the average energy-loss rate from an ergodic ensemble of atoms at a fixed energy and angular momentum. Similar classical averaging methods have been used by previous authors for both magnetized and unmagnetized Rydberg atoms.[13–15]

The average Larmor power at angular momentum $p_{\phi 0}$ and binding energy U_0 is

$$\left\langle\frac{\partial U}{\partial t}\right\rangle=\frac{2}{3}\frac{e^2}{c^3}\frac{\int\delta(p_\phi-p_{\phi 0})\,\delta(U-U_0)\ddot{\mathbf{x}}\cdot\ddot{\mathbf{x}}d^3xd^3p}{\int\delta(p_\phi-p_{\phi 0})\,\delta(U-U_0)d^3xd^3p}. \tag{59}$$

The integral in ϕ is trivial. The integral in p_ϕ sets $p_\phi=p_{\phi 0}$. We will hereafter omit the subscript 0 in $p_{\phi 0}$ with this understanding.

Since the radiation rate is independent of plasma parameters and depends only on atomic parameters, let us use the orbital ($\check{}$) units. In these units, Eq. (57) becomes

$$1=\frac{1}{(\check{\rho}^2+\check{z}^2)^{1/2}}-\frac{1}{2}\left[\check{p}_\rho^2+\check{p}_z^2+\left(\frac{\check{p}_\phi}{\check{\rho}}-\frac{1}{2}\check{\rho}\check{\Omega}_c\right)^2\right]\equiv\check{U}. \tag{60}$$

Now we can rewrite Eq. (59) as

$$\left\langle\frac{\partial U}{\partial t}\right\rangle=\frac{2}{3}\left(\frac{U}{mc^2}\right)^3\frac{U}{\mathcal{T}}\frac{\int\delta(\check{U}-1)\ddot{\check{\mathbf{x}}}\cdot\ddot{\check{\mathbf{x}}}d\check{\rho}d\check{p}_\rho d\check{z}d\check{p}_z}{\int\delta(\check{U}-1)d\check{\rho}d\check{p}_\rho d\check{z}d\check{p}_z}. \tag{61}$$

Above, $\mathcal{T}$ is a characteristic classical radiation time, defined as

$$\mathcal{T}\equiv\frac{e^2}{mc^3}=9.4\times 10^{-24}\ \mathrm{s}.$$

The Hamiltonian equations of motion provide $\ddot{\mathbf{x}}$. In dimensionless units,

$$\ddot{\check{\mathbf{x}}}=\left[-\frac{\check{\rho}}{(\check{\rho}^2+\check{z}^2)^{3/2}}+\check{\Omega}_c\left(\frac{\check{p}_\phi}{\check{\rho}}-\frac{1}{2}\check{\rho}\check{\Omega}_c\right)\right]\vec{a}_\rho+\check{\Omega}_c\check{p}_\rho\vec{a}_\phi-\frac{\check{z}}{(\check{\rho}^2+\check{z}^2)^{3/2}}\vec{a}_z, \tag{62}$$

where $\vec{a}_\alpha$ is the unit vector in the direction of coordinate α. Its dot product with itself is

$$\ddot{\check{\mathbf{x}}}\cdot\ddot{\check{\mathbf{x}}}=\frac{1}{(\check{\rho}^2+\check{z}^2)^2}-\frac{2\check{\Omega}_c}{(\check{\rho}^2+\check{z}^2)^{3/2}}\left(\check{p}_\phi-\frac{1}{2}\check{\rho}^2\check{\Omega}_c\right)+\check{\Omega}_c^2\left[\check{p}_\rho^2+\left(\frac{\check{p}_\phi}{\check{\rho}}-\frac{1}{2}\check{\rho}\check{\Omega}_c\right)^2\right]. \tag{63}$$

Substituting Eq. (63) into Eq. (61), we can carry out the integral analytically in all but the cylindrical radius:

$$\left\langle\frac{\partial U}{\partial t}\right\rangle=\frac{2}{3}\left(\frac{U}{mc^2}\right)^3\frac{U}{\mathcal{T}}F(\check{p}_\phi,\check{\Omega}_c), \tag{64}$$

where the dimensionless function F is given by

$$\begin{aligned}F(\check{p}_\phi,\check{\Omega}_c)=\frac{1}{\int_{\check{\rho}_{\min}}^{\check{\rho}_{\max}}\check{z}_{\max}d\check{\rho}}\int_{\check{\rho}_{\min}}^{\check{\rho}_{\max}}d\check{\rho}\Biggl\{&\frac{\check{z}_{\max}}{2\check{\rho}^2(\check{\rho}^2+\check{z}_{\max}^2)}+\frac{\arctan(\check{z}_{\max}/\check{\rho})}{2\check{\rho}^3}-2\check{\Omega}_c\check{z}_{\max}\frac{\check{p}_\phi-\frac{1}{2}\check{\rho}^2\check{\Omega}_c}{\check{\rho}^2(\check{\rho}^2+\check{z}_{\max}^2)^{1/2}}+\check{z}_{\max}\check{\Omega}_c^2\left(\frac{\check{p}_\phi}{\check{\rho}}-\frac{1}{2}\check{\rho}\check{\Omega}_c\right)^2\\&-\frac{\check{\Omega}_c^2}{2}\check{z}_{\max}\left[2+\left(\frac{\check{p}_\phi}{\check{\rho}}-\frac{1}{2}\check{\rho}\check{\Omega}_c\right)^2\right]+\frac{\check{\Omega}_c^2}{2}\left[\ln\left(\sqrt{\check{\rho}^2+\check{z}_{\max}^2}+\check{z}_{\max}\right)-\ln\left(\sqrt{\check{\rho}^2+\check{z}_{\max}^2}-\check{z}_{\max}\right)\right]\Biggr\},\end{aligned} \tag{65}$$

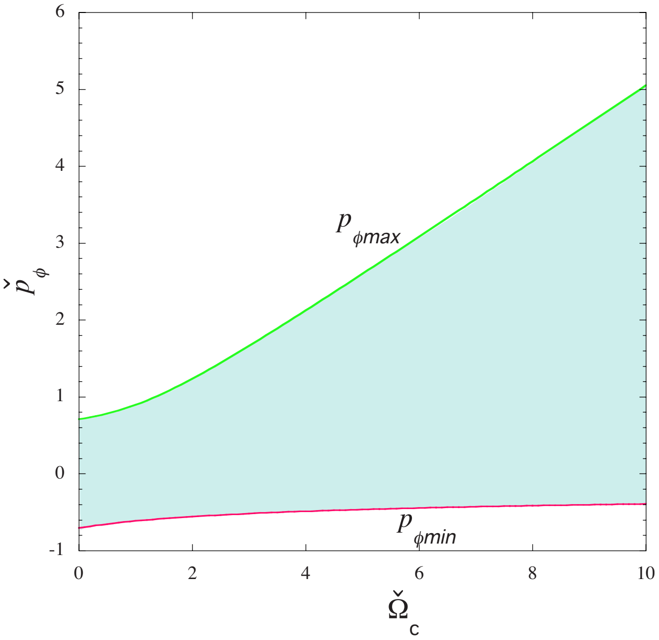

FIG. 15. (Color online) Allowed range of angular momentum for an atom with fixed binding energy, vs magnetic field.

and where

$$\check{z}_{\max} = \sqrt{4\left[2 + \left(\frac{\check{p}_\phi}{\check{\rho}} - \frac{1}{2}\check{\rho}\check{\Omega}_c\right)^2\right]^{-2} - \check{\rho}^2}$$

is the maximum accessible value of $\check{z}$ at the given value of $\check{\rho}$. Furthermore, $\check{\rho}_{\min}$ and $\check{\rho}_{\max}$ are the values of $\check{\rho}$ for which $\check{z}_{\max}$ vanishes, with $0 < \check{\rho}_{\min} < \check{\rho}_{\max} < 1$.

Solutions for $\check{\rho}_{\min}$ and $\check{\rho}_{\max}$ exist only for $\check{p}_\phi$ in the range $\check{p}_{\phi\min} < \check{p}_\phi < \check{p}_{\phi\max}$, where $\check{p}_{\phi\min}(\check{\Omega}_c)$ and $\check{p}_{\phi\max}(\check{\Omega}_c)$ are, respectively, the minimum and maximum values of scaled angular momentum at given binding energy and magnetic field. These two functions are plotted in Fig. 15. The orbits corresponding to $\check{p}_{\phi\min}$ and $\check{p}_{\phi\max}$ are circular orbits in the $z=0$ plane, moving clockwise and counterclockwise, respectively, when viewed from the positive z axis. At $\check{\Omega}_c=0$ (an unmagnetized atom), $\check{p}_{\phi\max} = -\check{p}_{\phi\min} = 1/\sqrt{2}$, and when $\check{\Omega}_c \gg 1$ (a strongly-magnetized atom), $\check{p}_{\phi\max} = \check{\Omega}_c/2$ and $\check{p}_{\phi\min} = -3(32\check{\Omega}_c)^{-1/3}$. In this strongly magnetized limit, the value of $\check{p}_{\phi\max}$ corresponds to a circular $\mathbf{E}\times\mathbf{B}$ drift orbit in the $z=0$ plane, and the value of $\check{p}_{\phi\min}$ corresponds to a circular cyclotron orbit, modified in frequency by the presence of the antiproton at the orbit's center.

In general, we must perform the integral in Eq. (65) numerically. Results of such calculations are presented in Fig. 16. However, a simplified expression is obtainable in the limit of small $\check{p}_\phi$. In this regime, radiative energy loss is dominated by close passes to the origin, for which the magnetic field has no significant impact. We may therefore take $\check{\Omega}_c=0$ in this regime. For the moment, however, let us leave the normalization factor $\int_{\check{\rho}_{\min}}^{\check{\rho}_{\max}} \check{z}_{\max} d\check{\rho}$ in its magnetic-field-dependent form but take the zero-field limit of the more complicated numerator. In the limit of small $\check{p}_\phi$, where orbits near the origin are allowed, the integral is dominated by small $\check{\rho}$. Equation (64) then simplifies greatly to

$$\left\langle \frac{\partial U}{\partial t} \right\rangle \approx \frac{2}{3}\left(\frac{U}{mc^2}\right)^3 \frac{U}{\mathcal{T}} \frac{1}{\int_{\check{\rho}_{\min}}^{\check{\rho}_{\max}} \check{z}_{\max} d\check{\rho}} \frac{3\pi}{8} \check{p}_\phi^{-4}. \tag{66}$$

Taking the zero-field, small $\check{p}_\phi$ limit of the normalization factor

$$\left.\int_{\check{\rho}_{\min}}^{\check{\rho}_{\max}} \check{z}_{\max} d\check{\rho}\right|_{\check{\Omega}_c=0,\check{p}_\phi=0} = \int_0^1 \sqrt{1-\check{\rho}^2}\, d\check{\rho} = \frac{\pi}{4},$$

simplifies the expression for the energy-loss rate:

$$\left\langle \frac{\partial U}{\partial t} \right\rangle \approx \left(\frac{U}{mc^2}\right)^3 \frac{U}{\mathcal{T}} \check{p}_\phi^{-4}. \tag{67}$$

The energy-loss rate diverges as $\check{p}_\phi^{-4}$, because for small $\check{p}_\phi$, the positron can make close passes to the antiproton. Low-

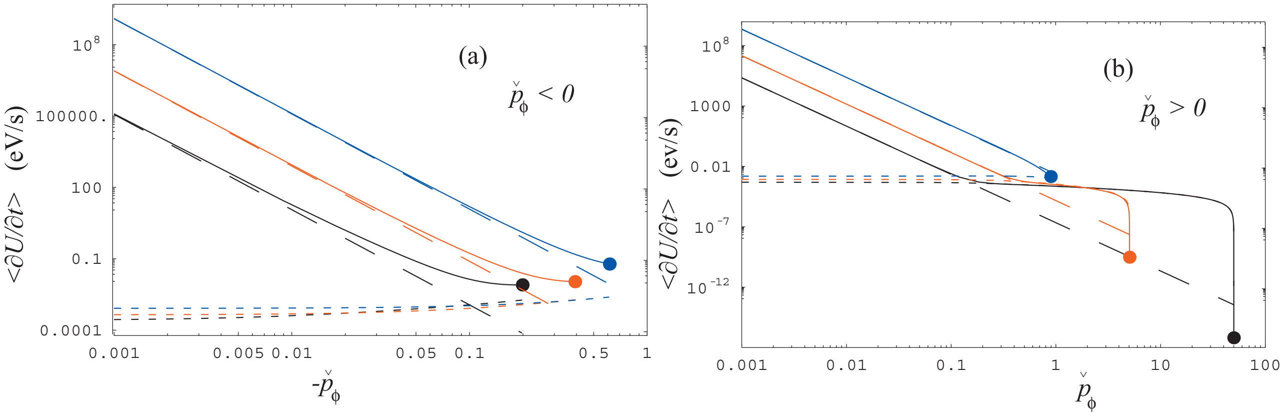

FIG. 16. (Color) The mean radiation rate $\langle \partial U/\partial t\rangle$ from Eq. (65) (solid curves) plotted against $\check{p}_\phi$ for a magnetic field of 1 T at three binding energies: $U=0.332$ meV (black), 1.54 meV (red), and 7.14 meV (blue), corresponding to $\check{\Omega}_c=100$, 10, and 1, respectively. Separate log-log plots are shown for (a) $\check{p}_\phi<0$ and (b) $\check{p}_\phi>0$. The dashed lines, proportional to p_ϕ^{-4}, estimate the rate in the region of strong radiation from Eq. (66). The dotted lines plot the rate omitting the electric force from Eq. (62) and represent cyclotron radiation. For large $\check{\Omega}_c$, cyclotron radiation dominates for all but the lowest angular momenta. At the chaotic cutoff ($\check{\Omega}_c=1$), all available states radiate more rapidly than the cyclotron level. The dots at the end of the solid curves are for circular orbits in the $z=0$ plane.

angular-momentum states radiate more rapidly to deeper binding.

Equation (67) differs from the well-known result for the classical energy-loss rate of an unmagnetized Rydberg atom because only p_ϕ and U are assumed to be conserved in Eq. (67), whereas other conserved quantities exist for an unmagnetized atom (i.e., the other components of angular momentum). If we were to hold these quantities fixed in the ergodic average, we would recover the result of Ref. 9 (p. 807).

At finite field, however, no simple analytic expression exists for the normalization factor. While the numerator is well approximated in the small $\check{p}_\phi$ region by the $\check{\Omega}_c=0$ case, the normalizing denominator exhibits $\check{\Omega}_c$ dependence. This dependence is a reflection of available phase space. At small $\check{p}_\phi$ and $\check{\Omega}_c \gg 1$, invariance of $\check{p}_\phi$ restricts orbits to small $\check{\rho}$. Zero-field ($\check{\Omega}_c=0$) orbits are not similarly restricted. We must use the more general equation (66) to approximate the strong radiation region (small $\check{p}_\phi$) for finite magnetic field.

Figure 16 shows the radiative energy-loss rate of Eq. (65) plotted against $\check{p}_\phi$ at three values of $\check{\Omega}_c$ in a 1 T magnetic field. At low $\check{p}_\phi$, the loss rate agrees with the $\check{p}_\phi^{-4}$ divergence given by Eq. (66). For large $\check{p}_\phi$ and large $\check{\Omega}_c$, the loss rate is dominated by cyclotron radiation. This can be seen by comparing the rates plotted in Fig. 16(b) at large $\check{p}_\phi$ to the dashed lines, which plot the rate obtained by omitting the electric force in Eq. (62), so that only cyclotron radiation is kept. In the guiding-center atom regime (high-$\check{\Omega}_c$), slowly radiating, high-$\check{p}_\phi$ states constitute much more of available phase space than in the chaotic regime. For such states, radiation is not an important effect. However, low-$\check{p}_\phi$ states (helical atoms) radiate much more rapidly.

In addition to transporting energy away from the atom, radiation also carries away angular momentum. We will use an ergodic average identical to that used in deriving the energy-loss rate of Eq. (65) to obtain an expression for the time rate of change of p_ϕ due to radiation. The instantaneous torque is given by

$$\frac{\partial p_\phi}{\partial t} = \mathbf{r} \times \mathbf{F}_{\text{rad}} \cdot \vec{a}_z,$$

where $\mathbf{F}_{\text{rad}}$ is the radiative reaction force, given by

$$\mathbf{F}_{\text{rad}} = \frac{2}{3}\frac{e^2}{mc^3} m\dddot{\mathbf{x}}.$$

Taking the derivative of Eq. (62) once in time and switching to dimensionless variables, the instantaneous radiative torque is

$$\frac{\partial p_\phi}{\partial t} = \frac{2}{3}\left(\frac{U}{mc^2}\right)^{3/2} U\check{\rho}\left(-\frac{\check{\rho}}{(\check{\rho}^2+\check{z}^2)^{3/2}}\dot{\check{\phi}} + \check{\Omega}_c\check{\rho}\dot{\check{\phi}}^2 - \check{\Omega}_c\dot{\check{p}}_\rho\right). \tag{68}$$

To express Eq. (68) in terms of coordinates and momenta only, we use the canonical definition of p_ϕ [Eq. (6)] along with the Hamiltonian relation

$$\dot{\check{p}}_\rho = \frac{\partial \check{U}}{\partial \check{\rho}}.$$

This gives the instantaneous torque in terms of phase variables $(\check{\rho}, \phi, \check{z}, \check{p}_\rho, \check{p}_\phi, \check{p}_z)$:

$$\frac{\partial p_\phi}{\partial t} = \frac{2}{3}\left(\frac{U}{mc^2}\right)^{3/2} U\left[\frac{\left(\frac{3}{2}\check{\rho}^2\check{\Omega}_c - \check{p}_\phi\right)}{(\check{\rho}^2+\check{z}^2)^{3/2}} + \check{\Omega}_c^2\left(\frac{1}{2}\check{\rho}^2\check{\Omega}_2 - \check{p}_\phi\right)\right]. \tag{69}$$

Once again presuming an ergodic orbit, we take a phase-space average over the distribution $\delta(U-U_0)\,\delta(p_\phi-p_{\phi 0})$ as in Eq. (59) to get the average rate of change of p_ϕ:

$$\left\langle \frac{\partial p_\phi}{\partial t}\right\rangle = \frac{2}{3}\left(\frac{U}{mc^2}\right)^{3/2} UG(\check{p}_\phi, \check{\Omega}_c), \tag{70}$$

where the dimensionless function G is given by

$$G(\check{p}_\phi, \check{\Omega}_c) = \frac{1}{\int_{\check{\rho}_{\text{min}}}^{\check{\rho}_{\text{max}}} d\check{\rho}\check{z}_{\text{max}}} \int_{\check{\rho}_{\text{min}}}^{\check{\rho}_{\text{max}}} d\check{\rho}\check{z}_{\text{max}} \times \left[\frac{\frac{3}{2}\check{\Omega}_c - \check{p}_\phi/\check{\rho}^2}{\sqrt{\check{\rho}^2+\check{z}_{\text{max}}^2}} + \check{\Omega}_c^2\left(\frac{1}{2}\check{\rho}^2\check{\Omega}_c - \check{p}_\phi\right)\right]. \tag{71}$$

While Eq. (71) gives the physical torque, we need to consider energy loss as well to find the rate of change of the rescaled $\check{p}_\phi$:

$$\left\langle \frac{\partial \check{p}_\phi}{\partial t}\right\rangle = \left\langle \frac{\partial}{\partial t}\frac{p_\phi}{e^2\sqrt{m_e/U}}\right\rangle = \frac{\langle \partial p_\phi/\partial t\rangle}{e^2\sqrt{m_e/U}} + \frac{1}{2}\check{p}_\phi\frac{\langle \partial U/\partial t\rangle}{U}. \tag{72}$$

This quantity, plotted in Fig. 17, has the same sign as $\check{p}_\phi$ for nearly the full range of $\check{p}_\phi$. Atoms thus evolve toward circular orbits in the $z=0$ plane, where $|\check{p}_\phi|$ is maximal. At small values of $\check{p}_\phi$, the first term, proportional to $\check{p}_\phi^{-1}$, is dominated by the second term, proportional to $\check{p}_\phi^{-3}$ [from Eq. (66)]. In this strong-radiation regime, torque is negligible, and orbits evolve toward circles in the $z=0$ plane as energy is radiated away.

Figure 18 shows two evolutions in U and $\check{p}_\phi$ predicted by Eqs. (65) and (72). For both low- and high-angular-momentum states, the rate of radiative relaxation accelerates near the chaotic regime. At small $\check{\Omega}_c$, the magnetic field no longer restricts the positron to an $\mathbf{E}\times\mathbf{B}$ drift orbit and the energy-loss rate of Eq. (65) approaches its unmagnetized value. This rate is proportional to U^4, evolving U to infinite energy in finite time. Concurrently, the radiative torque of Eq. (71) pushes the atom toward a circular orbit. When the initial angular momentum is small (indicating an eccentric orbit), the atom reaches deep binding before a circular orbit is established.

Note that the zero-field, small-angular-momentum energy-loss rate of Eq. (67), combined with $\langle \partial\check{p}_\phi/\partial t\rangle$ in the same limit,

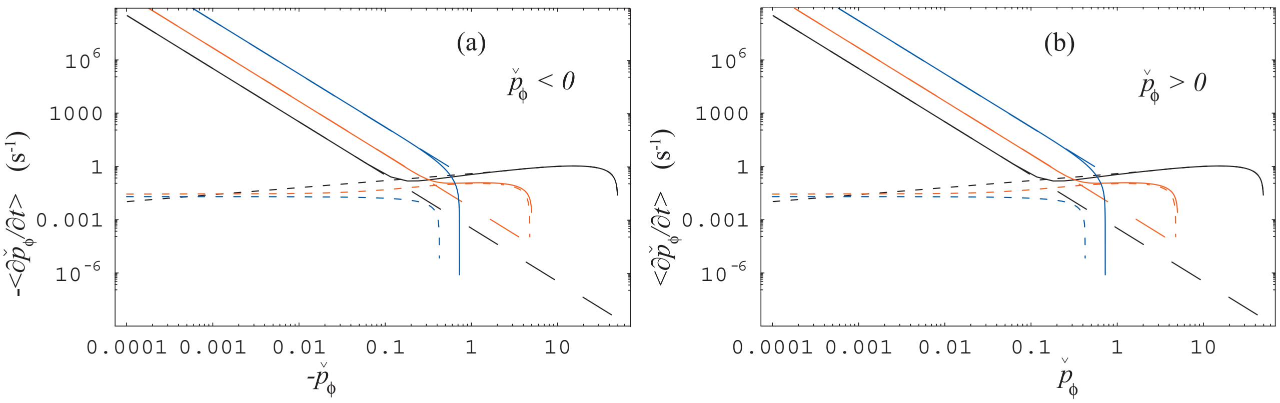

FIG. 17. (Color) The average change in $\check{p}_\phi$ due to radiation $\langle\partial\check{p}_\phi/\partial t\rangle$ [from Eq. (71), solid curves] plotted against $\check{p}_\phi$ for a magnetic field of 1 T at binding energies $U=0.332$ meV (black), 1.54 meV (red), and 7.14 meV (blue), corresponding to $\check{\Omega}_c=100$, 10, and 1, respectively. To accommodate log-log plots, (a) $\check{p}_\phi<0$, and (b) $\check{p}_\phi>0$ appear on seperate plots, with the sign of the vertical axis switched in the first case. Because $\check{p}_\phi$ includes energy in its definition, its rate of change includes an energy change contribution as well as physical torque. The dashed lines, proportional to $\check{p}_\phi^{-3}$, estimate $d\check{p}_\phi/dt$ in the region of strong radiation ($|\check{p}_\phi|\ll 0$), given by the second term in Eq. (72) and dominated by energy change. The dotted lines plot the torque due only to accelerations produced by the magnetic force (i.e., due to cyclotron radiation). Near the extreme values of $\check{p}_\phi$, the plotted quantity becomes negative (not shown).

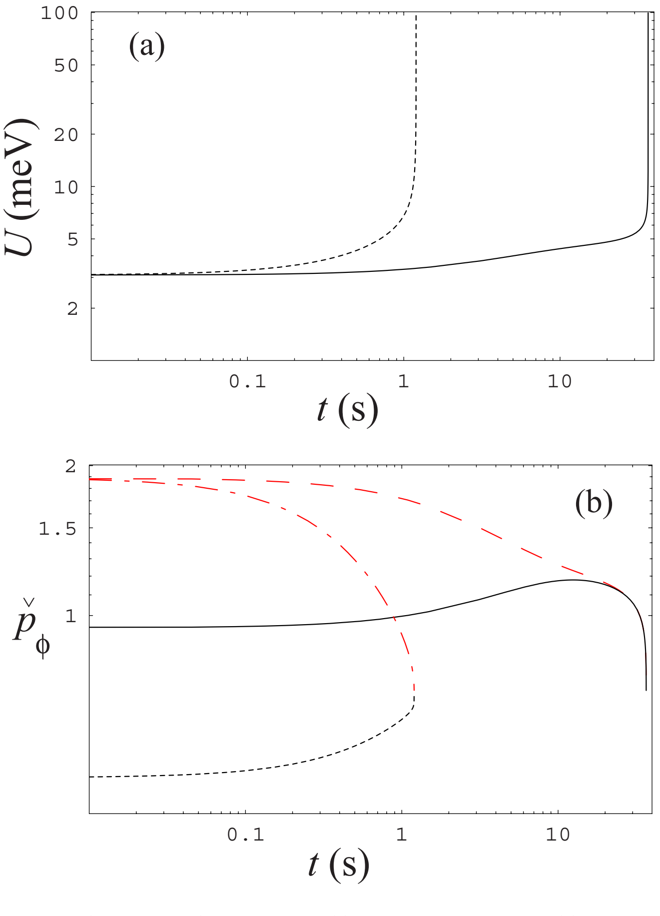

FIG. 18. (Color online) Evolution in (a) binding energy U and (b) rescaled angular momentum $\check{p}_\phi$ due to radiation for two atom initial conditions. The magnetic field is 1 T, and both atoms begin at $U=3.43$ meV ($\check{\Omega}_c=3.5$). The atoms are begun with $\check{p}_\phi=0.945$ (solid curves) and $\check{p}_\phi=0.472$ (dotted curves). In (b), the dashed and dot-dashed curves show the values $\check{p}_\phi=\check{p}_{\phi\,\mathrm{max}}$ that give (positively oriented) circular orbits for the higher and lower initial p_ϕ atoms, respectively. The higher-p_ϕ atom radiates to a slowly evolving, circular orbit before it reaches the chaotic cutoff energy (7.14 meV for a 1 T magnetic field). The lower-p_ϕ atom stays in an eccentric orbit through its evolution past the chaotic cutoff.

$$\langle\partial\check{p}_\phi/\partial t\rangle \approx \frac{1}{2}\left(\frac{U}{mc^2}\right)^3\frac{1}{\mathcal{T}}\check{p}_\phi^{-3}, \tag{73}$$

creates a system of differential equations in time with an analytic solution:

$$U(t) = \frac{U_0\check{p}_{\phi0}^4}{\check{p}_{\phi0}^4-(U_0/mc^2)^3(t/\mathcal{T})},$$
$$\check{p}_\phi(t) = \check{p}_{\phi0}\sqrt{\frac{U(t)}{U_0}}. \tag{74}$$

Scaled angular momentum $\check{p}_\phi$ grows without bound in this simple approximation, but the recombination time t_c (i.e., when the solution becomes singular), is still accurate for small initial $\check{p}_\phi$:

$$t_c = \mathcal{T}\left(\frac{mc^2}{U_0}\right)^3\check{p}_{\phi0}^4. \tag{75}$$

By neglecting the magnetic field, we obtain a result for the recombination time that is even in $\check{p}_\phi$. While the estimate is most applicable to orbits with an initially small angular momentum, Eq. (75) provides useful scaling for the recombination time with initial energy and angular momentum even near the extreme values of $\check{p}_\phi$ (circular orbits). Figure 19 shows the true recombination time found by simultaneously solving Eqs. (65) and (72) compared against the estimated t_c for two initial binding energies. For small $\check{p}_\phi$, the analytic approximation t_c works well. At larger angular momenta, the expression (66) underestimates the loss rate and the relaxation time is overestimated by t_c.

The recombination times plotted in Fig. 19 follow from a purely classical analysis. This analysis breaks down when the initial energy U_0 is near the ground state energy +13.6 eV or when the initial angular momentum is on the order of $\hbar$. While $U_0\ll 13.6$ eV in the cases considered here, the predicted p_ϕ^{-4} divergence in the energy-loss rate [Eq. (66)] is not physical when $p_\phi<\hbar$. This implies that there is a minimum recombination time set by quantum uncertainty in

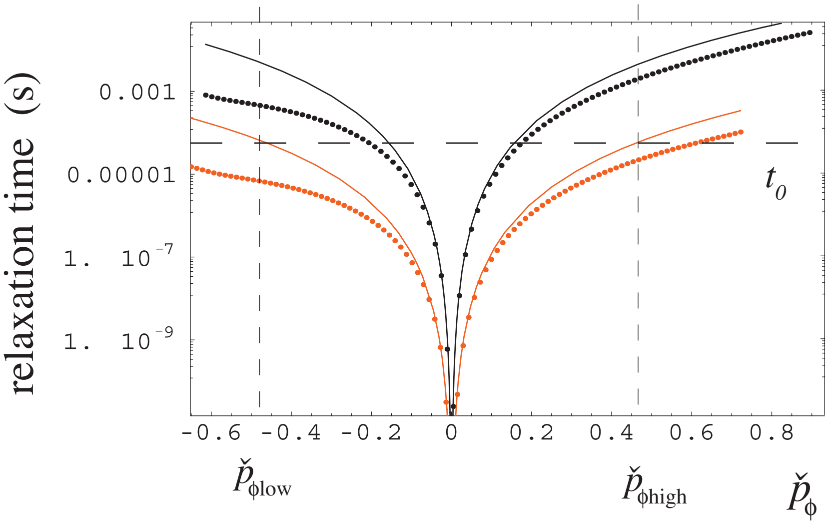

FIG. 19. (Color) The time to radiatively relax to the ground state based on ergodic average expressions (65) and (72) for the mutual evolution of energy U and rescaled angular momentum in the z direction $\check{p}_\phi$. The dots show when the solution becomes singular given the true evolution, while the curves show the small-$\check{p}_\phi$ approximation given by Eq. (75). Any given time t_0 defines a minimum and maximum $\check{p}_\phi$, defined for both the true and estimated evolutions, between which states will have relaxed to the ground state within t_0. A magnetic field of 6 T is assumed. The initial energies shown are $U_0=0.0236$ eV (the chaotic cutoff; black) and $U_0=0.1$ eV (red). The estimate maximum and minimum $\check{p}_\phi$ (determined from t_c) are illustrated for the $U=0.1$ eV case [see Eq. (77)].

the positron position, which may be estimated by replacing p_{ϕ_0} by $\beta\hbar$, where β is a factor of order unity in Eq. (75):

$$t_{c\min} = \mathcal{T}\left(\frac{mc^2}{U_0}\right)^3\left(\frac{\beta\hbar}{e^2\sqrt{m/U_0}}\right)^4 = \frac{1.68\beta^4\ \mu\text{s}}{U_0/1\ \text{meV}}. \qquad (76)$$

No state at energy U_0 can evolve to the ground state faster than $t_{c\min}$. The vast majority of states, having $p_\phi \gg \hbar$, will take much longer than $t_{c\min}$ to relax, as seen by the $\check{p}^4_{\phi0}$ dependence in Eq. (75).

If atoms radiate for a given time Δt starting at binding energy U, there exist low and high values of $\check{p}_\phi$, between which atoms will have fallen to the ground state (i.e., for which $t_c \leqslant \Delta t$). The estimated recombination time given in Eq. (75) is even in $\check{p}_\phi$, so the low and high values of $\check{p}_\phi$ have the same absolute magnitude:

$$\check{p}_{\phi\text{high}} = -\check{p}_{\phi\text{low}} = \left[\frac{\Delta t}{\mathcal{T}}\left(\frac{U_0}{mc^2}\right)^3\right]^{1/4}. \qquad (77)$$

By integrating an ergodic distribution in $\check{p}_\phi$ from $\check{p}_{\phi\text{low}}$ to $\check{p}_{\phi\text{high}}$, we may estimate the fraction of atoms that will radiatively relax after a given time.

Figure 20 shows the estimated times required for 10% and 50% of a distribution at energy associated with quantum number n to relax to the ground state in a 6 T magnetic field. The initial distribution is ergodic except for the restriction that $|p_\phi| > \hbar$ ($\beta=1$) and $|p_\phi| > 2\hbar$ ($\beta=2$), in keeping with the quantum estimate of Eq. (76). The results at 50% recombination are consistent with a quantum calculation performed by Topçu and Robicheaux.[16] The 10% results predict a recombination time five times faster than Ref. 16 for $n=35$ and $\beta=2$. The 10% recombination time depends sensitively on β because the depleted region of phase space ($|p_\phi| < \beta\hbar$) is of comparable volume to the volume of the radiating region. Quantum effects are most important in these low-p_ϕ states, and our result is only an order-of-magnitude estimate in this region.

Figure 21 shows the fraction combined after one collision time $(n\bar{v}b^2)^{-1}$ as a function of initial binding energy, given a 6 T magnetic field and a number density of 10^8 cm^{-3}. Three values of the *ad hoc* quantum parameter β [from Eq. (76)] are shown: $\beta=0$ (a fully classical point of comparison), $\beta=1$, and $\beta=2$. For $\beta=0$ (uppermost curve, black lines and dots), suppression of radiation below the chaotic cutoff is clearly visible. For the other cases, where p_ϕ is restricted to be larger than $\beta\hbar$, in keeping with the estimate of Eq. (76), the combined fraction is suppressed (middle

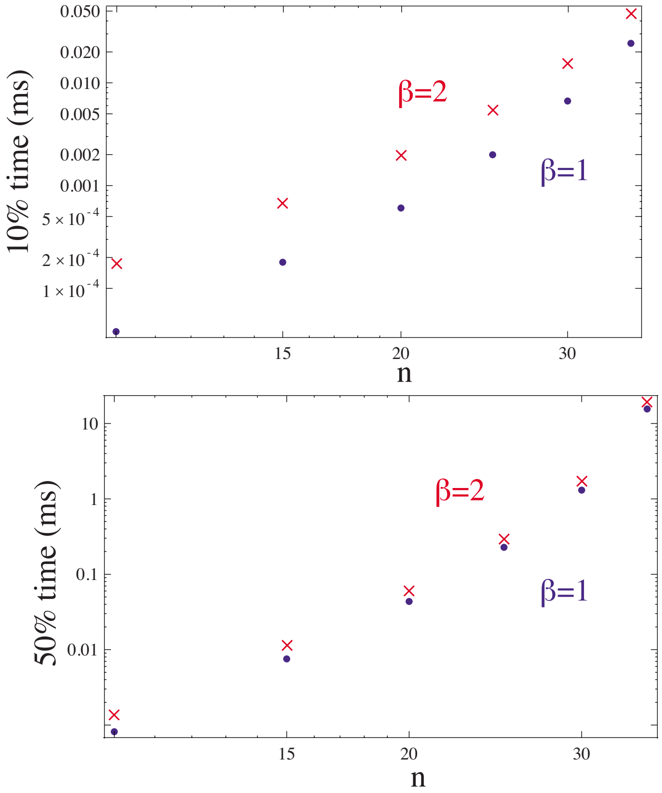

FIG. 20. (Color online) Estimated time required for 10% (a) and 50% (b) of states from an ergodic distribution at quantum number n ($U=13.6\ \text{eV}/n^2$) to relax to the ground state. Quantum effects are approximated by depleting the initial distribution for $|p_\phi| < \beta\hbar$. Dots and crosses are for $\beta=1$ and $\beta=2$, respectively.

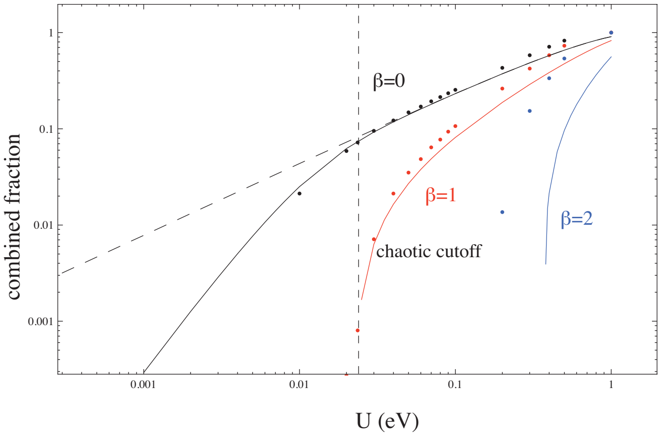

FIG. 21. (Color) The fraction of particles that would relax to the ground state after 0.074 μs (one collision time at 10^8 cm^{-3} and 4 K) as a function of initial energy, using a quantum estimate that requires $|p_\phi| > \beta\hbar$. The purely classical case is $\beta=0$ (black). The quantum estimates are $\beta=1$ (red) and $\beta=2$ (blue). The dots come from simultaneous solutions of Eqs. (65) and (72), while the lines use the estimated relaxation time t_c from Eq. (75). The dots and solid lines are for a magnetic field of 6 T. The dashed line is for the magnetic-field-free case. At energies smaller than the chaotic cutoff, the magnetic field reduces the recombined fraction below that for the unmagnetized case.

curve, red and blue lines and dots). One can see that the value of the quantum parameter is important, indicating that radiation is dominated by atoms with small p_ϕ and that a fully quantum calculation of the radiative recombination is necessary.[16] Our results, based on classical dynamics with an *ad hoc* quantum cutoff, can provide only an estimate of radiative effects.

With this caveat in mind, let us estimate the fraction of atoms that will relax to the ground state (due to radiation) from the collisional energy distributions previously determined. We assume that the radiating fraction is small, so that the distribution function $f(\epsilon)$ is not perturbed from the collisional one calculated earlier. (Later, we will discuss the limitations of this assumption.)

As radiation causes atoms with the lowest values of angular momentum $\check{p}_\phi$ to relax to the ground state, the ergodic distribution in angular momentum becomes depleted around $\check{p}_\phi=0$. At any particular energy, this "hole" in phase space widens as more time passes and the maximum angular momentum $\check{p}_{\phi\max}$ for which atoms will have relaxed increases. The number of atoms in the depleted region constitutes an estimate of the fraction of atoms in the ground state.

Consider the collisionally evolved distribution $f(\epsilon,t)$, calculated in the previous chapter. We now "turn on" radiation, allowing this distribution to radiatively relax for a period of time Δt. In this time some atoms at small angular momenta will fall to the ground state. We may ignore the simultaneous collisional evolution provided that we only consider short radiative relaxation times Δt compared to the total collisional evolution time $\tau/n\bar{v}b^2$. In this case, the number of atoms $N_{\mathrm{GS}}(t)$ radiatively relaxed to the ground state from a fixed distribution $f(\epsilon,t)$ after time Δt is

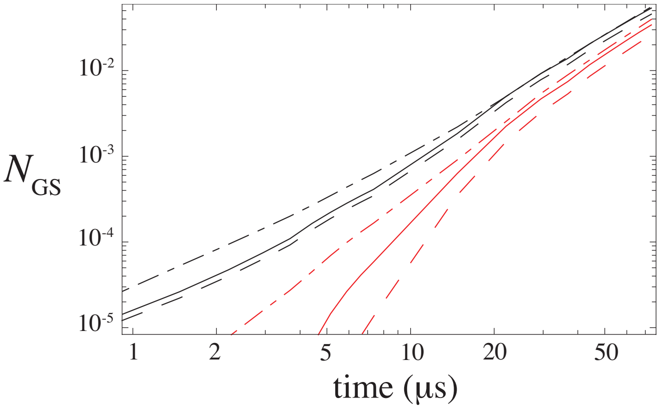

FIG. 22. (Color) The number of atoms N_{GS} that are estimated to reach the ground state per antiproton as a function of the transit time [Eq. (78)], using several methods. The black curves are purely classical estimates and the red curves include quantum effects by requiring $|p_\phi| > \hbar$. The magnetic field is 6 T, the temperature is 4 T, and the density is 10^8 cm^{-3}. The solid and dashed curves are obtained by allowing the collisionally evolved distribution after time t given by $f(\epsilon,t)$ to relax radiatively for a time Δt, where $\Delta t=0.1t$ and $\Delta t=0.05t$, respectively. The dot-dashed curves show an estimate if radiation is allowed to act continuously, and collisions are assumed to populate low-angular-momentum states. The requirement $|p_\phi| > \hbar$ (red curves) strongly reduces the ground state fraction at early times where atoms are weakly bound, but has less effect at later times where the collisional cascade has populated more deeply bound states, and the Stark-mixing time is longer.

$$N(t) = nb^3\left[\int f(\epsilon,t)\int_{\check{p}_{\phi\mathrm{low}}(\epsilon,\Delta t)}^{\check{p}_{\phi\mathrm{high}}(\epsilon,\Delta t)} P_{p_\phi}(\epsilon,\check{p}_\phi)\,d\check{p}_\phi\,d\epsilon + N_{100}(t)\int_{\check{p}_{\phi\mathrm{low}}(100,\Delta t)}^{\check{p}_{\phi\mathrm{high}}(100,\Delta t)} P_{p_\phi}(100,\check{p}_\phi)\,d\check{p}_\phi\right], \qquad (78)$$

where $P_{p_\phi}(\epsilon,\check{p}_\phi)$ is the ergodic probability of finding an atom with angular momentum $\check{p}_\phi$ at energy ϵ, given by Eq. (17). The second term in the integral above accounts for atoms that have passed $\epsilon=100$; i.e., the left boundary of the numerical solution of $f(\epsilon)$. N_{100} is the number of such atoms, all of which are assumed to lie at $\epsilon=100$ for purposes of radiation rate. Since $\check{p}_{\phi\mathrm{high}}$ and $\check{p}_{\phi\mathrm{low}}$ are proportional to $\Delta t^{1/4}$ [Eq. (77)], and $P_{p_\phi}(\epsilon,\check{p}_\phi)$ is peaked around $\check{p}_\phi=0$, a moderate change in relaxation time Δt has very little effect on the estimated number of atoms N in the ground state. The black curves in Fig. 22 show this estimate for two different choices of the radiative relaxation time Δt. The density is 10^8 cm^{-3} for all curves. As expected, the choice of Δt has little effect on the predicted number of ground state atoms formed.

To estimate quantum effects along the lines of the discussion surrounding Eq. (76), we also calculated $N(t)$ by setting $P_{p_\phi}(\epsilon,p_\phi)$ equal to zero for $|p_\phi| < \hbar$. This has a strong effect on N at early times when the mean binding energy is weak, because strong radiation occurs only for $|p_\phi| \lesssim \hbar$. This indicates that quantum effects cannot be ignored when determining radiative relaxation of such weakly bound states.

The previous estimates artificially turned on radiation for a time Δt. In actuality, radiation is acting during the entire collisional evolution. The radiation tends to depopulate low-$\check{p}_\phi$ states, and collisions tend to repopulate these states through Stark mixing.[17,18] Let us estimate this effect by breaking it into a two-step process: beginning with a collisionally evolved distribution $f(\epsilon,t)$, ergodically distributed in p_ϕ, radiation depopulates the low-p_ϕ states in a time Δt, creating a hole in the distribution. The hole is then filled in by Stark mixing, and the distribution also evolves in energy according to the previous collisional calculation. This assumes that the fraction of p_ϕ states depopulated by radiation is small, so that the radiation has only a negligible effect on the collisionally evolved distribution calculated previously. For Δt, we then choose the time required to fill in the hole by Stark mixing. We estimate this time as

$$\Delta t = \frac{\epsilon^2}{n\bar{v}b^2}. \tag{79}$$

This time is longer for atoms at deep binding because such atoms have a smaller collisional cross section. This is roughly the scale on which the energy distribution evolves collisionally (see Fig. 12), and we assume that the angular momentum distribution evolves on the same timescale. This estimate clearly requires verification through more detailed analysis.

In this crude model, the number of atoms $\mathcal{N}_{\mathrm{GS}}(\epsilon,t)$ that reach the ground state in time t from energy ϵ is

$$\mathcal{N}_{\mathrm{GS}}(\epsilon,t) = \sum_{m=0}^{t/\Delta t} \int_{\check{p}_{\phi\mathrm{low}}(\epsilon,\Delta t)}^{\check{p}_{\phi\mathrm{high}}(\epsilon,\Delta t)} d\check{p}_\phi P_{p_\phi}(\epsilon,\check{p}_\phi) f(\epsilon,m\Delta t) nb^3.$$

For small Δt, this can be rewritten as

$$\mathcal{N}_{\mathrm{GS}}(\epsilon,t) = \frac{nb^3}{\Delta t} \int_{\check{p}_{\phi\mathrm{low}}(\epsilon,\Delta t)}^{\check{p}_{\phi\mathrm{high}}(\epsilon,\Delta t)} P_{p_\phi}(\epsilon,\check{p}_\phi) d\check{p}_\phi \int_0^t f(\epsilon,t')dt'.$$

For deep binding, Δt grows large and can exceed the total evolution time t. To account for this, we must take the smaller of t or Δt in the denominator of the prefactor above. With this consideration, the total number of atoms in the ground state is given by the integral over ϵ. Switching the time integration variable from t' to $\tau = t' n\bar{v}b^2 = t'\nu$ and using the estimate for Δt from Eq. (79), the number $N_{\mathrm{GS}}(t)$ is

$$\begin{aligned} N_{\mathrm{GS}}(t) = nb^3 \Bigg[\int \frac{1}{\mathrm{Min}(\epsilon^2,t\nu)} \int_{\check{p}_{\phi\mathrm{low}}(\epsilon,\Delta t)}^{\check{p}_{\phi\mathrm{high}}(\epsilon,\Delta t)} P_{p_\phi}(\epsilon,\check{p}_\phi) d\check{p}_\phi \\ \times \int_0^{t\nu} f(\epsilon,\tau) d\tau d\epsilon + \frac{1}{t\nu} \int_{\check{p}_{\phi\mathrm{low}}(100,\Delta t)}^{\check{p}_{\phi\mathrm{high}}(100,\Delta t)} d\check{p}_\phi \\ \times P_{p_\phi}(100,\check{p}_\phi) \int_0^{t\nu} N_{100}(\tau) d\tau \Bigg]. \end{aligned} \tag{80}$$

As before, all atoms that have cascaded deeper than $\epsilon = 100$ are considered to be at this energy.

As before, we evaluate Eq. (80) using a pure classical model, as well as a quantum estimate by setting $P_{p_\phi} = 0$ for $|p_\phi| < \hbar$. The two results for the fraction of atoms in the ground state are shown by the black and red dot-dashed lines in Fig. 22. The quantum estimate yields a much lower combined fraction at short times where the collisional cascade has only populated weakly bound states. At longer times, where more strongly bound states are collisionally populated, radiation from states with $p_\phi > \hbar$ plays an important role. For long transit times, deep binding is reached through collisional de-excitation and radiation overtakes collisional energy loss. For deeply bound atoms, the radiatively depopulated hole around $\check{p}_\phi = 0$ now encompasses a large fraction of available phase space, and the Stark mixing time is long. Most such atoms relax quickly to the ground state, so the hole is only filled in when atoms cascade from more shallow binding.

The previous argument should be taken only as a crude estimate of the effect of Stark mixing on the radiative recombination rate. A more rigorous examination of this issue requires solution of the master equation for the evolution of a distribution in both ϵ and p_ϕ, including radiative depopulation of the low-p_ϕ states and collisional repopulation of these states, and including quantum effects. This important but computationally intensive problem will be the subject of future work.

IX. CONCLUSIONS

A numerical solution of the master equation for collisional evolution of the energy distribution of weakly bound antihydrogen atoms in a cold positron plasma was obtained using a transition probability rate density derived from a classical Monte-Carlo simulation. Only transitions in atomic binding energy were considered in the solution, with all other variables assumed to fill an ergodic distribution. This approximation was justified by numerically evaluated atomic orbits, and by agreement between the master equation solution and a time-consuming simulation where no such approximation was made.

The approximation of ergodic orbits was shown to apply well over all investigated binding energies. Ergodic phase-space distributions differ qualitatively between guiding-center drift atoms and chaotic atoms. In the first case, the cyclotron action provides an additional constant of the motion and modifies the distribution from the fully ergodic, three-dimensional form seen in chaotic atoms. At each binding energy, atom orbits were found to qualitatively fill the appropriate distribution. This had important consequences for magnetic confinement of antihydrogen. An increase in the number of low magnetic field seeking states was seen to accompany the shift from guiding-center atoms to chaotic atoms (Fig. 4). This shift improves prospects for magnetic confinement of charge-neutral antihydrogen once deeper binding is reached.

The master equation solution shows that the distribution in energy evolves collisionally to a nearly flat, steady-state value with a power-law tail. The steady state is rapidly established at binding energies weaker than the kinetic bottleneck, then progresses slowly to deeper binding, reaching the chaotic cutoff in a few hundred to a few thousand collision times. The flux of atoms to deeper binding is constant in the steady-state region (but not in the power-law tail) and scales with temperature as expected;[5] i.e., as $T^{-9/2}$. However, antihydrogen atoms observed in experiments lie in the tail, not in the steady-state region, so their formation rate does not match the steady-state value. In particular, the scaling of this rate with plasma temperature depends strongly on antiproton transit time, and is much less dependent on temperature than the steady-state flux, as seen in Fig. 14.

The estimated rate of radiative energy loss, also in the classical approximation, was used to predict the number of atoms that relax to the ground state. Only atoms with chaotic orbits, due either to low angular momentum (helical atoms) or deep binding, radiate significantly. The fraction of atoms where the collisional cascade to deep binding is outpaced by radiative energy loss increases with deeper binding, especially as the chaotic cutoff energy ϵ_c is reached. Collisional Stark mixing enhances this capture rate by repopulating rapidly radiating, low-angular-momentum states, but quantum effects limit the radiative rate. For an antiproton transit time of 10 μs through a 4 K positron plasma with density of 10^8 cm^{-3} and a magnetic field of 6 T, our crude estimates predict that around one antiproton transit in 10 000 will result in a ground-state atom (see the red, dot-dashed curve in Fig. 22).

The radiation rate depends sensitively on angular momentum as well as energy, implying that a more rigorous determination of the angular momentum distribution will be needed in the future. Such a determination requires a more comprehensive solution of the master equation, preserving evolution in both energy and angular momentum, to correctly characterize the distribution of angular momenta during the collisional cascade. In addition, a quantum calculation of the radiative energy loss similar to Ref. 16 must be combined with the collisionally evolved distribution in order to properly account for radiation from states with angular momenta of order $\hbar$. This computationally intensive but important problem will be the subject of future work.

ACKNOWLEDGMENTS

The authors acknowledge useful discussions with Professor T. M. O'Neil and Professor C. F. Driscoll.

This work was supported by National Science Foundation Grant No. PHY-0354979 and NSF/DOE Grant No. PHY-0613740.

[1] M. Amoretti, C. Amsler, G. Bonomi, A. Bouchta, P. Bowe, C. Carraro, C. L. Cesar, M. Charlton, M. J. T. Collier, M. Doser, V. Filippini, K. S. Fine, A. Fontana, M. C. Fujiwara, R. Funakoshi, P. Genova, J. S. Hangst, R. S. Hayano, M. H. Holzscheiter, L. V. Jørgensen, V. Lagomarsino, R. Landua, D. Lindelöf, E. Lodi Rizzini, M. Macrì, N. Madsen, G. Manuzio, M. Marchesotti, P. Montagna, H. Pruys, C. Regenfus, P. Riedler, J. Rochet, A. Rotondi, G. Rouleau, G. Testera, A. Variola, T. L. Watson, and D. P. van der Werf, Nature (London) **419**, 456 (2002).

[2] G. Gabrielse, N. S. Bowden, P. Oxley, A. Speck, C. H. Storry, J. N. Tan, M. Wessels, D. Grzonka, W. Oelert, G. Schepers, T. Sefzick, J. Walz, H. Pittner, T. W. Hänsch, and E. A. Hessels, Phys. Rev. Lett. **89**, 213401 (2002).

[3] P. Mansbach and J. Keck, Phys. Rev. **181**, 275 (1969).

[4] M. E. Glinsky and T. M. O'Neil, Phys. Fluids B **3**, 1279 (1991).

[5] F. Robicheaux and J. D. Hanson, Phys. Rev. A **69**, 010701 (2004).

[6] T. Pohl, H. R. Sadeghpour, and G. Gabrielse, Phys. Rev. Lett. **97**, 143401 (2006).

[7] E. M. Bass and D. H. E. Dubin, Phys. Plasmas **11**, 1240 (2004).

[8] H. Kono, T. Tazaki, I. Kawata, and Y. Fujimura, J. Chem. Phys. **111**, 10895 (1999).

[9] J. D. Jackson, *Classical Electrodynamics*, 2nd ed. (John Wiley & Sons, New York, 1999).

[10] F. Robicheaux, Phys. Rev. A **73**, 033401 (2006).

[11] M. E. Glinsky, T. M. O'Neil, and M. N. Rosenbluth, Phys. Fluids B **4**, 1156 (1992).

[12] C. F. Driscoll, Phys. Rev. Lett. **92**, 149303 (2004).

[13] M. R. Flannery and D. Vrinceanu, Phys. Rev. A **68**, 030502 (2003).

[14] J. R. Guest, J.-H. Choi, and G. Raithel, Phys. Rev. A **68**, 022509 (2003).

[15] M. W. Horbatsch, E. A. Hessels, and M. Horbatsch, Phys. Rev. A **72**, 033405 (2005).

[16] T. Topçu and F. Robicheaux, Phys. Rev. A **73**, 043405 (2006).

[17] S. K. Dutta, D. Feldbaum, A. Walz-Flannigan, J. R. Guest, and G. Raithel, Phys. Rev. Lett. **86**, 3993 (2001).

[18] D. Vrinceanu and M. R. Flannery, Phys. Rev. Lett. **85**, 4880 (2000).